

Application of Scanning Tunneling Microscopy and Spectroscopy in the Studies of Colloidal Quantum Qots

Jiaying Duan,^[a] Jiapeng Wang,^[a] Liangpeng Hou,^[a] Peixuan Ji,^[a] Wusheng Zhang,^[a] Jin Liu,^[a] Xiaodong Zhu,^[a] Zhixiang Sun,^[b] Yanqing Ma,^[a] and Lei Ma^{*[a]}

Abstract: Colloidal quantum dots display remarkable optical and electrical characteristics with the potential for extensive applications in contemporary nanotechnology. As an ideal instrument for examining surface topography and local density of states (LDOS) at an atomic scale, scanning tunneling microscopy (STM) and scanning tunneling spectroscopy (STS) has become indispensable approaches to gain better understanding of their physical properties. This article presents a comprehensive review of the research advancements in measuring the electronic orbits and corresponding energy levels of colloidal quantum dots in various systems using STM and STS. The first three sections introduce the basic principles of colloidal quantum dots synthesis and the fundamental methodology of STM research on quantum dots. The fourth section explores the latest progress in the application of STM for colloidal quantum dot studies. Finally, a summary and prospective is presented.

Keywords: colloidal quantum dots, scanning tunneling spectroscopy, local density of states, electronic structure

1. Introduction

Quantum dots (QDs) are semiconductor nanocrystals that confine conduction band electrons, valence band holes and excitons in three spatial dimensions. The carrier movement in QDs is limited in three-dimensional space, so QDs are also known as “artificial atoms”, “super-atoms” or “quantum dot atoms”, with sizes ranging from 1 to 100 nm.^[1–4] QDs can be considered as a bridge between small molecules and bulk crystals. They have discrete electronic transition states like isolated atoms and molecules, as well as the properties of crystalline materials.^[5–10] According to the material composition, QDs can be classified into single element QDs, compound QDs and heterojunction QDs. They can be also divided into colloidal QDs and solid self-assembled QDs based

on their existence state. Because of the characteristics of energy level separation, size adjustability and strong light stability,^[5,6,11–17] high fluorescence efficiency and high absorption value of unit incident fluorescence, QDs have been gradually applied to solar cells,^[18–20] photodetectors,^[21–25] biomedicine^[26–30] and many other fields. Colloidal QDs have become the first choice for the study of optical and electrical properties in QD systems owing to their low cost and easy control of components.^[6,31–33]

A primary objective in nanoscience is to establish direct connection between the structure of materials (molecules, nanocrystals), electronic properties and photoelectric functions, which could make full use of their physical properties and complete QDs functionalities.^[34] Additionally, in the self-assembled superlattice structure, it is necessary to associate the characteristics of a single nanocrystal with the macroscopic properties of the overall structure.^[35] Among the traditional QD research methods, optical measurement methods have the advantages of high photon energy and high resolution, such as absorption spectrum and photoluminescence spectrum, but they reveal the result of the average effect of the size and shape of QDs in the segment. Consequently, precise correlations

[a] J. Duan, J. Wang, L. Hou, P. Ji, W. Zhang, J. Liu, X. Zhu, Y. Ma, L. Ma

Tianjin International Center for Nanoparticles and NanoSystems, Tianjin University, Tianjin, China, 300072

E-mail: Lei.ma@tju.edu.cn

[b] Z. Sun

Center for Joint Quantum Studies and Department of Physics, School of Science, Tianjin University, Tianjin, China, 300072

between QD properties and their specific topography and size remain elusive. Scanning tunneling microscopy (STM) and scanning tunneling spectroscopy (STS) provide essential tools for addressing this challenge. These techniques enable atomic-resolution imaging of colloidal quantum dots and simultaneous measurement of electrical properties, including local density of electronic states, spatial electron cloud distribution, and charge transport characteristics. Because of its ultra-high spatial and energy resolution, STM and STS have emerged as highly effective methods to study nanomaterials.^[36–38]

In the past three decades, STM and STS have been extensively used in the study of electronic structures of single nanostructures, for instance, single atoms,^[39–42] atomic vacancies,^[43] molecules,^[44–46] and clusters such as C₆₀^[47,48] while achieved a series of remarkable results. In 1999, Banin et al.^[49] first studied InAs colloidal QDs by combining STM and optical measurements. Single-electron multiple states of the QDs were observed in tunneling spectrum that the energy level spacing was consistent with the optical transition results. This groundbreaking study provided an intuitive understanding of the internal single-electron energy level structure of semiconductor nanocrystals and the electron-electron and electron-phonon interaction, sparking a surge of interest in STM research on colloidal nanocrystals.^[50–58] Since then, researchers have used STM to explore properties of colloidal QDs, mainly focusing on the effects of size and shape regulation of colloidal QDs on their properties,^[49,58,59] the coupling between dots in colloidal QDs arrays,^[34,35,60,61] the surface properties of colloidal QDs^[62–64] and heterostructures.^[58,65] These results have greatly deepened the understanding of the photoelectric properties of colloidal QDs, and rapidly promoted the applications of colloidal QDs in optoelectronic devices, biological detection, medical imaging, and other fields.

By controlling the geometric shape and size of colloidal QDs to alter their electronic state structures, thereby “tailoring” the electrical and optical properties of QDs, is an essential component of “bandgap engineering” and a frontier research hotspot worldwide. At present, there are many related reviews of colloidal QDs.^[66–69] As the colloidal synthesis techniques of functional nanostructures are advancing at a fast pace, people have made great progress in the properties and applications of colloidal QDs. Table 1 summarizes the latest progress in the field of colloidal QDs. Colloidal QDs develop rapidly. Through the study of their surface structure and electrical properties by STM, the intrinsic physical properties can be understood more deeply, and then widely used in various fields. The purpose of this review is to systematically summarize the application of STM in colloidal QDs.

In this review, the application of STM and STS in colloidal QDs is systematically discussed. The first three sections introduce colloidal QDs, and a theoretical basis to understand

STM and STS on QDs attached to a conducting surface. The subsequent section summarizes the research progress of STM in various colloidal QD systems. Finally, we discuss the open problems can be addressed by STM techniques in colloidal QDs and the future development of colloidal QDs in the field of nanoscience.

2. Overview of Colloidal Quantum Dots

Among the various QD materials, colloidal QDs are the largest category.^[86] Colloidal QDs are usually synthesized and processed in solution and are composed of small size nanocrystals and surface organic ligands. Their dimensions are generally smaller than the exciton Bohr radius of the bulk materials. The surface organic ligands are usually composed of long-chain aliphatic acids or aliphatic amines, which form a coating on the nanocrystal surfaces.^[25,87,88]

Compared with other types of QDs, colloidal QDs have the following advantages: 1) The size of QDs can be accurately controlled, the average size distribution is about 5%–10%, and QDs with small enough particle size can be synthesized to obtain strong quantum confinement effect; 2) Because surface ligands can stabilize colloidal QDs, allowing for their uniform dispersion in organic solvents and thus facilitating the characterization of the intrinsic properties of individual QDs; 3) The preparation of high-density QD arrays can be easily realized to study the coupling effect between dots; 4) Compared with other technologies (take for example molecular beam epitaxy), the chemical synthesis method of colloidal QDs has low cost and is easy to prepare on an industrial scale. It has high versatility in terms of size, composition, shape, and surface modification.^[89–95] Next, we will briefly introduce the synthesis methods and basic properties of typical colloidal QDs.

2.1. Synthesis of Colloidal QDs

In the early stages of QD development during the 1980s, QD synthesis relied on traditional chemical methods for preparing colloidal particles, such as coprecipitation, microemulsion, and micelle techniques. These methods generally use water-soluble salts as precursors to prepare QDs by direct reaction with ligand stabilizers (e.g., mercapto alcohol, mercapto acid, mercaptoamine and mercapto amino acid) or by heating and refluxing in the presence of a certain concentration of ligand stabilizers.^[96] However, the QDs synthesized by aqueous phase method have some defects, e.g. low fluorescence efficiency, wide particle size distribution and poor crystallization. Moreover, simple sulfhydryl compounds have poor stability and tend to fall off from the surface of QDs, leading to QDs aggregation. In contrast, the organic phase synthesis method is widely used in the synthesis of semiconductor colloidal QDs.

Table 1. The latest progress in the field of colloidal QDs.

QDs	Field	Year	Method	Results	Properties	Ref.
III–V QDs	Synthesize	2021	Suppression of monomer	InAs QDs size over 9.0 nm (first)	the first peak of the InAs QDs appeared at 1600 nm, with 12.2% size distribution	[70]
		2023	Cation exchange	High-quality wurtzite InAs NCs (first)	quantum yield of up to ~37%	[71]
	Surface modifications	2021	Gas-phase deposition	n-type charge transport of InAs QD films	higher electron mobilities.	[72]
		2022	Hybrid ligand-exchange strategy	n-doping of InP QD films	average electron mobility ~0.45 cm ² V ⁻¹	[73]
	Application	2019	BP as transport layer	InP QDs photodetector	responsivity ~1 × 10 ⁹ A/W detectivity ~4.5 × 10 ¹⁶ Jones	[74]
			p-NiO as hole transport layer Nb: TiO ₂ as electron transport layer	In(As, P) QDs-based photodetector	photosensitive up to 1400 nm	[75]
		2022	amphoteric dual passivation strategy	InAs QD photodiodes	EDE ~30% at 940 nm	[76]
		2022	insert a hole-transporting semiconductor	InAs core/shell NIR-range LED	quantum yield ~73% device EQE ~13%.	[77]
PbX QDs	Synthesize	2021	biomimetic strategy	PbS NPs	crystallization and uniform distribution	[78]
		2019	two-step ligand-exchange method	increase PbS QDs ligand-exchange ratio	PbS QDs-based photodetector responsivity increase 94%	[79]
	Application	2022	PbSe QD Superlattice Transistors	microscale field-effect transistors	detectivity enhancement 57% hole mobility ~3.5 cm ² V ⁻¹ s ⁻¹ at 290 K ~6.5 cm ² V ⁻¹ s ⁻¹ at 170–220 K	[80]
		2022	sintered PbSe/PbS heterojunction	Mid-Infrared metamaterial enhanced heterostructure photodetector	responsivities ~375 at a wavelength of 2710 nm ~4.8 A/W at 4250 nm	[81]
		2023	introduce polyimide	large-area flexible PbS QD photodiodes	detectivity > 10 ¹³	[82]
Heterostructure Application	2021	in-situ surface passivation	PbSe QD/ZnO heterostructure NIR photodetectors	NIR R ~970 mA/W D* ~1.86 × 10 ¹¹ Jones	[83]	
		Bismuth sulfide electron transport layer	HgTe Infrared Photodetectors	dark current density ~1.6 × 10 ⁻⁵ A/cm ²	[84]	
	2022	two deposited layers active material	n-type PbS QDs/p-type carbon nanotubes light-emitting field-effect transistors	charge carrier mobility ~0.2 cm ² V ⁻¹ s ⁻¹	[85]	

Through screening organic solvents and precursors with high boiling point, the QDs with good crystallinity, uniform size and good dispersion are obtained.^[97] In 1993, Bawendi research group^[97] reported the first high-quality QD with continuously adjustable size (1.2–11.5 nm) and excellent optical properties, with the title of “Synthesis and characterization of nearly monodisperse CdE (E = sulfur, selenium, tellurium) semiconductor nanocrystallites”. The QDs have good crystal structures, surface properties and high size monodispersity. Figure 1 shows the sketch of the synthesis of QDs by hot injection method. With trioctylphosphine oxide (TOPO) and trioctylphosphine (TOP) as organic solvent and

ligands, dimethyl cadmium as cadmium source, and (TMS)₂E (E = S, Se, Te) as anion source, the cadmium source and anion source are mixed in the glove box and then taken out and quickly injected into the high-temperature organic solvent, and high-quality CdE (E = S, Se, Te) colloidal QDs are successfully prepared. The key points of synthesis established in this experiment include phosphine sulfur element precursors, ligand-protected metal precursors, hot injection rapid nucleation, separation of nucleation and growth processes, separation and purification of QDs, which have been adopted and improved in many subsequent works. This synthesis work successfully realizes the continuous control of the size and

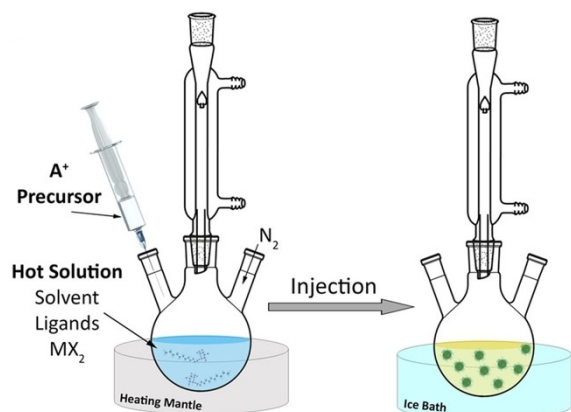


Figure 1. Sketch of the hot injection method used for the synthesis of colloidal QDs.^[103] This figure is taken from Ref. [103] with permission.

optical properties of QDs for the first time. Researchers in relevant fields have “seen” the charm of quantum confinement effect. This synthesis work significantly impacted both fundamental research and technical applications, greatly advancing nanotechnology development. However, the synthesis route selected dimethyl cadmium which is high toxicity, high cost and unstable room temperature, thus limited its application in the future.^[98] In 2001, Peng et al. found that the core reaction path of the above method is the reaction of dimethyl cadmium with organic phosphonic acid impurities in TOPO to produce organic cadmium phosphonate and then react with Se to produce CdSe, so the real precursor is organic cadmium phosphonate. They improved above traditional methods, and selected CdO instead of dimethyl cadmium as the precursor of Cd to synthesize high-quality CdS, CdSe, CdTe QDs in one step.^[99,100] In the following year, they proposed the non-coordination solvent approach, introducing non-coordination solvent, octadecene (ODE).^[101] This method effectively avoids the use of organic cadmium, without the requirement of anhydrous and oxygen-free conditions. And it

has the advantages of mild reaction, fast nucleation speed, and good experimental repeatability, to realize the true “green synthesis route” of QDs. The emergence of this synthesis route has greatly promoted the development of QDs. Since then, the development of the synthesis method of QDs has entered a fast lane. In 2005, Mulvaney et al. used the reaction of Se powder and ODE as the source of Se, which further improved the reaction activity and conversion, and simplified the preparation method, which has unique advantages in the synthesis of QDs with complex structure.^[102]

The formation of QDs involves two steps: nucleation and growth.^[104] During the synthesis process of QDs, the precursor is rapidly injected into high-temperature organic solvent, which makes the monomer concentration rapidly increase and exceed the nucleation value, thus inducing explosive nucleation. Since the significant consumption of monomer, its concentration rapidly decreases to below the nucleation threshold and stops further nucleation, thus entering the nucleation growth stage. The growth stage is mainly carried out by reaction control growth and diffusion control growth. First, the monomer diffuses to the surface of the QD, and then the monomer reacts with the surface of the QD to grow. The two ways exist simultaneously. When the monomer concentration is very high, the diffusion process is fast, and the reaction-controlled growth is dominant, and vice versa. As a result, by adjusting the amount of injected precursor to adjust the monomer concentration, QDs of different shapes, such as rod-shaped quantum dots, quantum quadrangle frames, can be synthesized.^[105,106] When the monomer concentration is too high, the monomer diffuses to each crystal plane quickly, so the reaction speed between monomer and crystal plane becomes the decisive step, which is the process of reaction-controlled growth. The growth rate of each crystal plane is different, so the topography is asymmetric, as shown in Figure 2 below. When the concentration of monomer is low, the diffusion speed of monomer to each crystal plane is slow, while the reaction speed between monomer and crystal plane is fast, and the growth process is diffusion-controlled growth, so

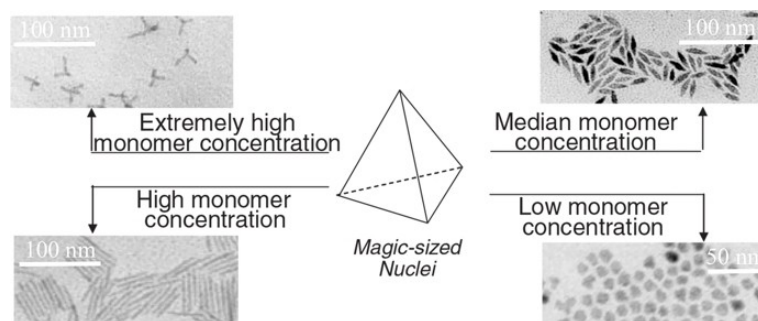


Figure 2. Monomer-concentration-dependent growth paths of CdSe nanocrystals.^[106] This figure is taken from Ref. [106] with permission.

the growth of each crystal plane tends to be uniform, and the topography of the synthesized QDs is spherical-like.

Single component QDs have high surface activity, which makes them easy to agglomerate, and many defects on the surface will affect the performance of QDs. Consequently, people focus on the research of core/shell heterostructure nanocrystals. By selecting a semiconductor material as the core and coating another shell material on its surface, the stability, dispersion, and luminescence characteristics of QDs can be improved. In 1996, it was reported for the first time that ZnS-coated CdSe QDs were synthesized by organometallic reagents. Under the condition of keeping the size of CdSe unchanged, ZnS with high bandgap width was directly grown on almost monodisperse CdSe.^[107] The key to the synthesis of core/shell structure nanocrystals is how to add the shell precursor to the core particle solution to avoid its own homogeneous nucleation in the solution. The method based on cadmium chalcogenide can also be used to synthesize other common semiconductor core/shell heterostructure nanocrystals. In the core/shell structure QDs, the shell grows epitaxial on different plane of the core crystal, resulting in the passivation of the core interface. This passivation is not simply accomplished by organic ligands. As consequence, the quantum yield of photoluminescence of the core/shell structure nanocrystals can be as high as 50–90%, and the photochemical stability is also improved.

2.2. Properties of Colloidal QDs

The unique properties of QDs come from the quantum effects. When the particle size enters the nanometer scale, the carrier movement is limited, and the quantum effects are significant, resulting in the evolution of its semiconductor energy band structure into a discrete energy level structure like atomic, showing many physical and chemical properties different from macroscopic bulk materials, for instance surface effect, quantum confinement effect, and Coulomb blockade effect.

2.2.1. Surface Effect

Surface effect refers to that with the decrease of the size of QDs, the specific surface area increases significantly. Most of the atoms are located on the surface of QDs. There are many dangling bonds and unsaturated bonds on the surface of low coordination, resulting in high activity and instability of the surface, making QDs prone to clustering.^[67,108,109] Figure 3 shows the relation between the surface atomic ratio of CdSe QDs and their size. As shown in Figure 3, with the decrease of the QD diameter, the proportion of surface atoms increases. Depending to its size, 10%–80% of all its atoms are located on the surface, which increases the surface defects, thus affecting the fluorescence efficiency and fluorescence lifetime

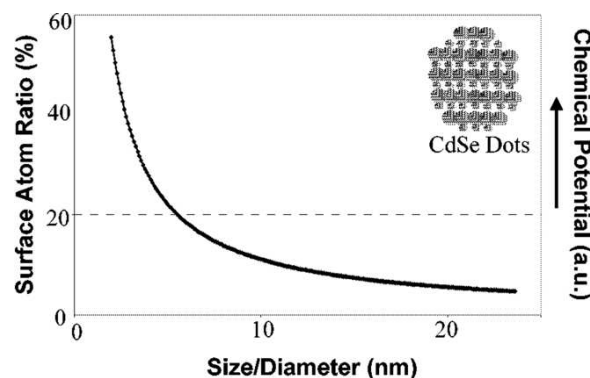


Figure 3. Size-dependence of the surface atom ratio and the relative chemical potential of CdSe nanocrystals, assuming a spherical shape.^[101] This figure is taken from Ref. [101] with permission.

of the QD.^[110] The increase of suspension bonds leads to the increase of surface free energy and surface activity of QDs, which makes the QDs attract each other and lose their excellent solution properties. To eliminate the influence of surface suspension bond, the surface of the QD needs to be modified. In this process, organic ligands typically bind to surface-suspended bonds in the form of bonds. Typical ligands include TOP, TOPO, oleic acid, and various fatty amines (e.g., oleamine, octylamine, etc.). Ligands reduce surface defects, electrons and holes can be more effectively combined by emitting light, and the luminescence of QDs can be improved.

2.2.2. Quantum Confinement Effect

When the photon energy absorbed by the semiconductor material is greater than its bandgap width, the electrons in the valence band are excited to the conduction band, and a hole is generated in the valence band. Under the Coulomb interaction, the electron-hole attracted by each other is symmetrical as an exciton. When the size of the semiconductor material is smaller than the Bohr radius of the exciton, the motion of the electron is limited in space, and the quasi-continuous energy band of the semiconductor material will change into a discrete energy level structure, which is the quantum confinement effect.^[5,111–114] Electronic and hole states with symmetries of S, P, D and F appear in spherical QDs. Figure 4(a) shows the influence of QD size on energy level structure. With the decrease of QD size, the bandgap increases continuously, resulting in the change of absorption spectrum of QD. Figure 4(b) shows the influence of the size of CdSe QDs on the absorption spectrum. As the size of the QD decreases, the light absorption spectrum moves to the short-wave direction.^[5,69]

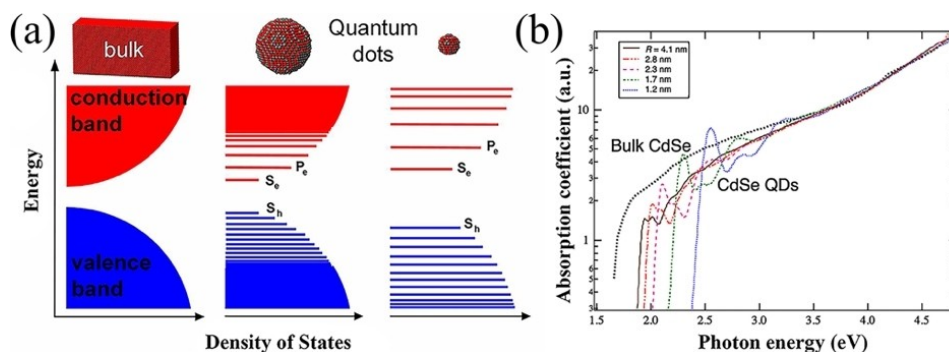


Figure 4. (a) Evolution of the electronic structure of inorganic semiconductors from bulk material to QDs of different size.^[115] These figures are taken from Ref. [115] with permission. (b) Absorption spectra of CdSe QDs with mean radii from 1.2 to 4.1 nm in comparison to the absorption spectrum of bulk CdSe multiplied.^[69] These figures are taken from Ref. [69] with permission.

2.2.3. Coulomb Blockade Effect

When the capacitance of a single QD is small enough, the QD increases the electrostatic energy of an electron by more than its thermal energy. This electrostatic energy will prevent a second subsequent electron with similar energy from entering the same QD, a phenomenon known as Coulomb blocking. The single electron tunneling process can be realized by using the Coulomb blockade effect.

3. Scanning Tunneling Microscopy

3.1. Scanning Tunneling Microscopy/Spectroscopy

Since its invention in 1981, STM has rapidly become one of the important technologies in the field of nanoelectronics and surface science. STM is based on the following principles. First, the basic principle of STM is quantum tunneling effect. When bias voltage is applied between the tip and the sample and the tip is very close to the sample surface, electrons can tunnel through the vacuum barrier and generate tunneling current. Second, the piezoelectric effect, which allows precise control of the xyz direction on the angstrom scale to approach or move away from the sample on a very small scale. Finally, a feedback loop is established to change the distance between the STM tip and the sample by adjusting the bias voltage or tunneling current.

Taking the advantage of its atomic resolution, STM can not only image the surface of the sample, but also study the LDOS of the sample through STS. The LDOS of samples studied by STS is based on the general expression of tunneling current:

$$I_t = \frac{4\pi e}{\hbar} \int \rho_s(\epsilon) \rho_t(\epsilon - eV) [f(\epsilon - eV) - f(\epsilon)] |M|^2 d\epsilon \quad (1)$$

$|M|^2$ is the tunneling matrix element, determined by the wave function of the sample and tip, ρ_s and ρ_t is the LDOS of the sample and tip respectively, $f(\epsilon)$ is fermi distribution function. Considering that the temperature broadening is relatively small relative to the energy resolution of the experiment, the Fermi distribution function can be replaced by a step function,

$$f(\epsilon - eV) - f(\epsilon) = \begin{cases} 0, \epsilon < 0 \\ 1, 0 < \epsilon < eV \\ 0, \epsilon > eV \end{cases} \quad (2)$$

The state density of the sample can be obtained by selecting the tip whose state density is constant within a certain bias voltage range. Consequently, the tunneling current can be further simplified as:

$$I_t \propto \int_0^{eV} \rho_s(\epsilon) d\epsilon \quad (3)$$

The derivation of the above formula for the bias voltage can be obtained as follows:

$$\frac{dI_t}{dV} \propto \rho_s(eV) \quad (4)$$

Differential conductivity dI/dV of the tunneling current is proportional to the LDOS of the sample. So, the LDOS of the sample can be obtained by measuring the $I(V)$ curve and calculating the differential conductivity dI/dV . The dI/dV spectrum obtained by this method has great noise and cannot give useful information, so usually the dI/dV signal is measured directly with a phase-locked amplifier. Add a small cosine modulation signal $V_m \sin(\omega t)$ to the applied bias voltage

so that the tunneling current changes with the modulation signal,

$$I_t(V, V_m \sin \omega t) = I_0 + \frac{dI_t(V)}{dV} \cdot V_m \sin(\omega t) + \frac{1}{2} \frac{d^2 I_t(V)}{dV^2} \cdot V_m^2 \sin^2(\omega t) + \dots \quad (5)$$

I_0 is the tunneling current without modulated signal. Using phase-locked technology can significantly improve the sensitivity of measurement.

3.2. Preparation of QDs/Substrate Samples

When using STM to study QDs, the preparation of substrate/QD samples is the key to obtain the topography and tunneling spectrum. Colloidal nanocrystals are suspended, so a suitable substrate is needed to carry QDs to make them stable. There are two methods commonly used: (1) A bifunctional organic linker connects a single QD to the substrate^[49,116] (usually flat Au (111) surface), this method is mostly used to study single QDs. (2) The QDs suspended in the organic solution are spun or dripped onto a flat conductive substrate, such as highly oriented pyrolytic graphite (HOPG) or noble metal single crystal substrate, to form a self-assembled superlattice structure. The first method was first applied, for example, self-assembled nanostructured superlattices composed of Au^[117] and CdSe^[95] nanocrystals, but it has limitations. The second method is more common, for example single-layer array of CdSe QDs,^[118] PbSe QDs^[34] dispersed in CdSe array, single PbSe QDs^[60] and InAs QD array.^[119]

In the preparation of substrate/QD samples, the super-clean surface is the key to the successful preparation. It is required not to have many free solvents and ligand molecules. The adsorption on the tip will directly change the vacuum tunneling barrier, thus affecting the experimental results. The

“tip-QD-substrate” junction must be mechanically stable, which is more difficult to achieve than self-assembled solid QDs. Accordingly, when the sample is sent into the ultra-high vacuum chamber of the STM, the annealing method is usually used to evaporate the loosely bound molecules and stabilize the “QD-substrate” junction. The ligand molecules with several nanometer-long and stable binding QDs have significant HOMO-LUMO energy gap, and their function is equivalent to a potential barrier in the process of electron tunneling. The structure of “tip-QD-substrate” can be described by a model of double barrier tunneling junction (DBTJ). Its schematic diagram and equivalent circuit are shown in Figure 5.

3.3. Double Barrier Tunneling Junction

When using STM to study colloidal QDs, a DBTJ of “tip-QD-substrate” will be formed. In this geometry, in addition to the energy level structure of the QDs, the parameters of the two junctions, especially the capacitance (C_t and C_s) and the tunneling resistance ($R_{\text{tip/QD}}$ and $R_{\text{QD/sub}}$), have a great impact on the tunneling spectrum.^[54,56,121,122] On one hand, the capacitance and tunneling resistance (C_t and $R_{\text{tip/QD}}$) of the tip-QD junction (inversely proportional to the tunneling rate) are affected by the tip-QD distance (usually by controlling the STM bias voltage and current). On the other hand, the parameters of the QD-substrate junction (C_s and $R_{\text{QD/sub}}$) are determined by the properties of the QD itself and the chemical connection of the substrate and can be controlled by adjusting the experimental parameters. A detailed understanding of the role played by the DBTJ geometry is essential to correctly explain the tunneling properties of QDs. The barrier between the tip and QD consists of vacuum gaps and ligand molecules, while the barrier between the QD and the substrate is mainly ligand molecules. The electron tunneling from tip to substrate consists of two tunneling processes, namely, the tunneling between the tip and the QD

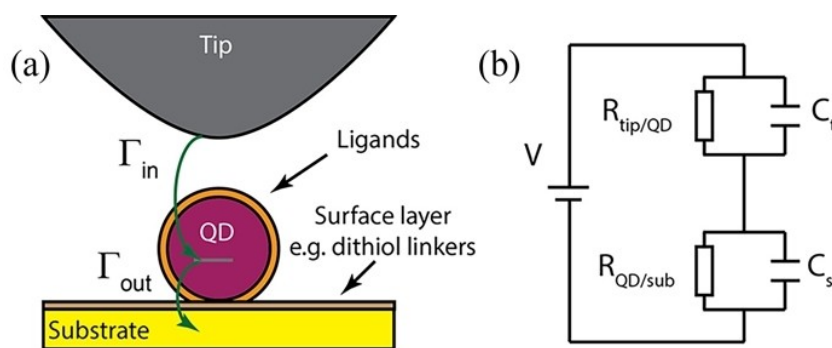


Figure 5. Double barrier tunneling junction. (a) The tip-QD-substrate system contains two tunneling barriers. (b) The equivalent electric circuit of the double-barrier tunneling junction, $V (=V_{\text{substrate}} - V_{\text{tip}})$ stands for the applied bias voltage between the substrate and the tip.^[120] These figures are taken from Ref. [120] with permission.

and the tunneling between the QD and the substrate. These two processes have a certain tunneling probability respectively Γ_{in} , Γ_{out} (number of electrons passing through the tunneling junction per unit time). When the Fermi level at the tip resonates with the energy level in the QD, the tunneling channel opens. For a given positive (negative) bias voltage, the ratio Γ_{in}/Γ_{out} will determine the number of additional electrons (holes) in the QD. By varying the distance between the tip and QD the magnitude of the tunneling current can be changed, and it is possible to produce two kinds of tunneling spectra: “shell-tunneling” spectra and “shell-filling” spectra.^[123]

When the tunneling current is very small, the probability of electrons (holes) tunneling into QDs is far less than the probability of tunneling out of QDs, electrons (holes) tunnel through the nano-object one-by-one and electron-electron interactions do not occur (Figure 6a). In this case, the tunneling spectra directly reflects the single-electron density of states of QDs, which is called “shell-tunneling” spectra.

Under the “shell-tunneling” condition, the first electron can be added to the QD when the Fermi level at the tip aligns with the S_e level, which can be expressed as,

$$\eta V_b = \epsilon_s^e + \Sigma_{pol} \quad (6)$$

V_b is the bias voltage applied between the tip and substrate, η is a voltage lever arm, which depends on the radius of curvature of the tip and the dielectric constant of the QD, ϵ_s^e is the energy of the S_e energy level of the QD, Σ_{pol} is the electrostatic polarization energy required to add an extra electron to the S_e energy level of the QD, which is affected by the charge shielding of the tip and substrate.^[5,121,124,125]

When the first hole is added to the QD,

$$\eta V_b = \epsilon_s^h - \Sigma_{pol} \quad (7)$$

Under positive bias voltage, there is no current flow in the potential region between the first electron resonance and the first hole resonance under negative bias voltage, so the

tunneling conductance is zero, then the zero-conductance gap measured by STM is,

$$\eta \cdot V_g = \epsilon_s^e - \epsilon_s^h + 2\Sigma_{pol} \quad (8)$$

Under positive bias voltage, electrons can tunnel into the P_e level,

$$\eta V_b = \epsilon_p^e + \Sigma_{pol} \quad (9)$$

The distance between the first peak and the second peak in the “shell-tunneling” spectra directly gives the energy difference between the energy levels S_e and P_e .

By reducing the distance between the tip and the QD, the tunneling current is gradually increased. When it reaches or exceeds a critical value, Γ_{in} more than Γ_{out} , the energy level of the QD will be occupied by multiple carriers (Figure 6b). In QDs, one electron enters another before going out, and more energy is needed to overcome the mutual repulsion energy between electrons. The measured spectrum is called “shell-filling” spectra.

When the second electron tunneling to the S_e level of the QD, the energy level degeneracy increases,

$$\eta V_b = \epsilon_s^e + \Sigma_{pol} + \epsilon_{ee} \quad (10)$$

ϵ_{ee} is the coulomb repulsion energy between the added electrons.^[5,121,124–126] The energy level of S_e in the tunneling spectra shows a double peak, and the coulomb interaction energy between electrons can be obtained by the distance between the two peaks.

The QD band gap measured by STM is compared with the measured optically,

$$\Delta E_{opt} = \epsilon_s^e - \epsilon_s^h + 2\Sigma_{pol} + \epsilon_{ch} = \cdot E_{STM} + \epsilon_{ch} \quad (11)$$

ϵ_{ch} is the mutual attraction energy between electrons and holes. All energy levels of QDs, the degeneracy of single-electron

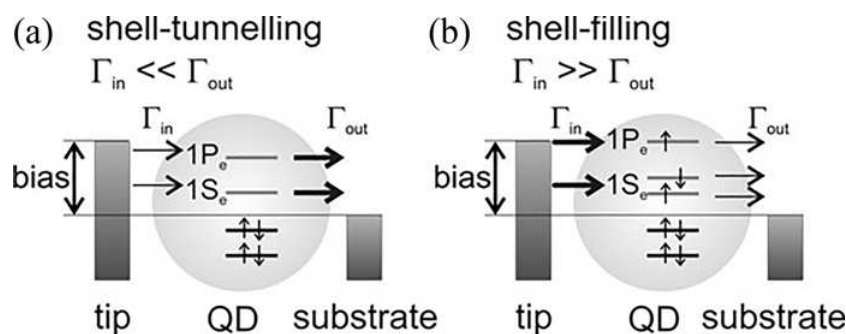


Figure 6. Schematics of (a) shell-tunnelling and (b) shell-filling spectroscopy.^[122] These figures are taken from Ref. [122] with permission.

eigenstates and the eigenstates produced by Coulomb interaction can be directly measured in the STS.

In experiments, the “shell-filling” region is difficult to reach owing to the instability of the tunneling junction and the shielding of the tip against the strong charge. If the tip-QD distance reduction results in a symmetrical distribution of tunneling barriers (η close to 0.5), the energy levels of the QDs change considerably relative to their positions at zero bias voltage. This may lead to bipolar charge transfer and tunneling spectra becomes complex.^[46,120,122,127]

3.4. Comparison of Scanning Tunneling Spectroscopy and Optical Spectroscopy

The principles of optical measurement and STS are different. Combining them to analyze semiconductor nanocrystals from different angles can provide a more comprehensive understanding of their electrical properties. In the absorption spectrum, the electrons in the valence band absorb radiation and then transition to the conduction band. The photoluminescence spectrum is that after the colloidal QDs absorb the excited photon energy, the electrons in the valence band jump to the conduction band and will soon release energy and then jump back to the valence band. Due to the relaxation process of excited QDs, the energy of emitted photons may be slightly different from that of absorbed photons. Using optical technology to detect the electronic transition between the energy levels of QDs needs to follow the necessary selection rules. Not all energy levels are reflected in optical resonance. Furthermore, the spatial resolution of spectroscopy is limited to a quarter of the wavelength of light, it is usually not possible to investigate a single nanocrystal, except in the special case of a two-dimensional system with highly diluted molecules or QDs.^[122,128–131] The electronic states of conduction band and valence band can be obtained by STM, and the information about the LDOS can be directly obtained by measuring the dI/dV curve of a single QD. Furthermore, the optical measurement mainly obtains the information of the electronic allowable transition with high oscillation intensity in QDs, and the STS can realize the direct measurement of the energy level of semiconductor QDs.^[122] Therefore, STS can effectively supplement the electronic properties of QDs that are not detected in optical measurement, to obtain more abundant information.

4. Application of Scanning Tunneling Microscope in Colloidal Quantum Dots

With high spatial and energy resolution, STM can not only be used to characterize the surface structure, but also accurately measure the local electrical properties of the sample through

STS. This provides a powerful way to study the electrical properties of semiconductor nanocrystals,^[25,132,133] which plays an important role in the study of the electrical properties of colloidal QDs.

4.1. III–V Quantum Dots

4.1.1. Energy Level Structure of a Single Colloidal QD

In 1999, Banin et al.^[49] studied InAs colloidal QDs by combining STM and optical measurement for the first time. InAs QDs with a radius of 1–4 nm are adsorbed on the surface of Au substrate by hexane dithiol molecule, and the stepwise distribution I–V curve is obtained by STM tip directly above the QDs at 4.2 K, as shown in Figure 7(a) below. The first two peaks and the next six equally spaced peaks in the tunneling spectrum shown in Figure 7(b) correspond to the two-peak and six-peak structures formed by the splitting of the S_c and P_c states of the QDs, respectively, while the energy difference between the two peaks in the S_c and P_c states corresponds to the mutual repulsion energy between the electrons. The zero current region corresponds to the sum of the band gap E_g between the conduction band and the valence band of the QD and the Coulomb interaction energy E_c . From the size dependence of QD tunneling spectrum shown in Figure 7(c), we can see that with the decrease of QD size, the band gap and the energy gap between S_c and P_c states increase nonlinearly, which is a typical quantum confinement effect. Figure 7(d–e) shows the comparison between STS and photoluminescence excitation spectrum. From Figure 7(d), there is a certain difference between the E_g value obtained by STS and optical spectrum. This is mainly caused by the electron-hole interaction. After the above correction, the results measured by the two methods shown in Figure 7(e) show good consistency.

In addition to the study of the intrinsic properties of InAs single points, Banin and Millo et al.^[134] used STM to measure the InAs QDs doped with Au, Ag and Cu. The results in Figure 8 showed that the tunneling spectra of the QDs doped with metal changed significantly. For example, when doping Au, although the band gap of InAs QDs is like that before doping, the characteristic peaks of QDs are covered up, indicating that the doping of Au destroys the original energy level structure of QDs. A direct consequence of bulk semiconductors doping is the Fermi level shift. Such shifts are distinctly observed in STS of Cu- and Ag-doped QDs. In the undoped case, the Fermi energy is nearly centered, whereas in the Cu-doped case, the onset of the conduction band states nearly coincides with the Fermi energy, consistent with n-type doping (Figure 8, blue trace). In case of Ag doping, since it has a large radius that is considered to be a substitutional impurity in III–V semiconductors. When the substitution of an

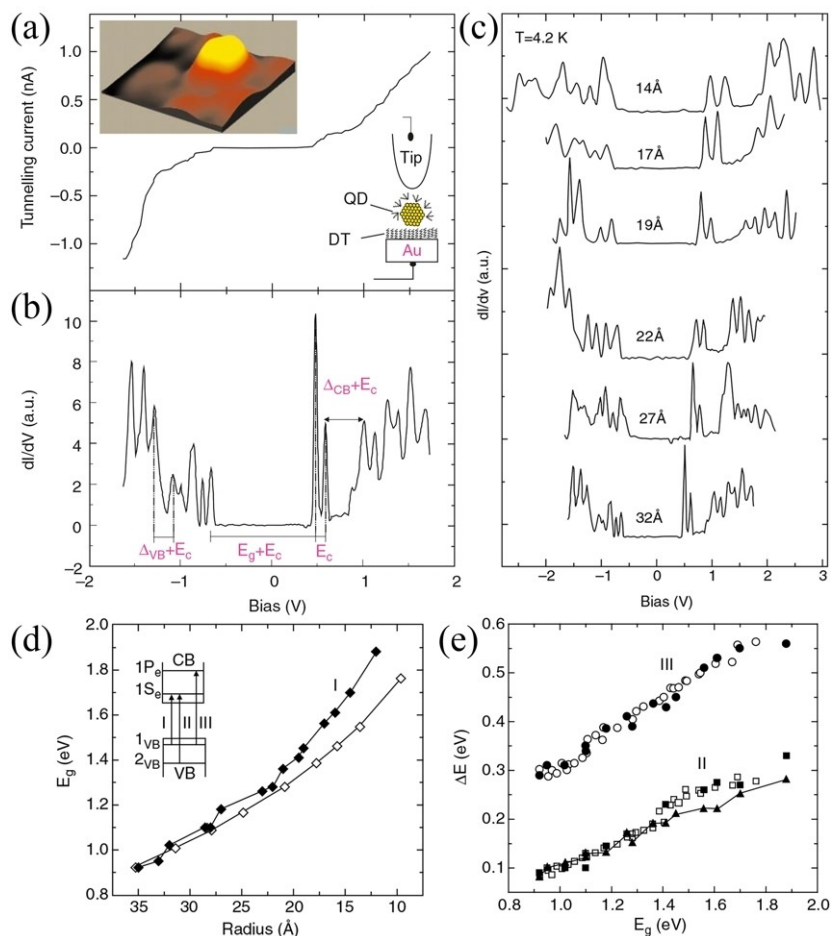


Figure 7. STM and STS of a single InAs QD 3.2 nm in radius, acquired at 4.2 K. (a) The tunnelling I–V characteristic. (b) The tunnelling conductance spectrum, dI/dV versus V , obtained by numerical differentiation of the I–V curve. (c) Size evolution of representative tunnelling dI/dV versus V characteristics, displaced vertically. (d) Comparison of the size dependence of the low-temperature optical bandgap (transition I) from which the excitonic Coulomb interaction was subtracted (open diamonds), with the bandgap measured by the STM (filled diamonds). (e) Plot of excited transitions versus the bandgap for tunnelling and optical spectroscopy.^[49] These figures are taken from Ref. [49] with permission.

indium atom with three valence electrons by a single valence electron Ag atom will lead to p-type doping due to the two electrons deficiency in the bonding orbitals. This is reflected in the shift of the Fermi level, as seen in the STS data (Figure 8, red trace). This method of controllable synthesis of n-type and p-type doped QDs provides good guidance for the research and development of various electronic and optoelectronic devices.

Surface ligands can control the dispersion stability and aggregation of colloidal QDs.^[104] Ligands have many functions, including the dissolution of precursors and the control of the size, shape, and dispersion of QDs. Moreover, ligands usually also affect the surface chemical composition,^[135] optical and electrical properties,^[136–140] functionality and processability of QDs.^[141,142] STM can effectively observe the surface structure of QDs and extract the structure and conformation

information of surface ligands. Michal et al.^[143] studied the influence of ligand exchange reactions on valence band energy levels of InAs QDs using STM. Figure 9 shows the effect of 4-methylthiophenol (MTP) and aniline exchange TOP as ligands on the tunneling spectra of InAs QDs with a diameter of about 4.4 nm. It is shown that the band gap does not change with the exchange of ligands, which confirms the results of optical measurement. At the same time, the energy band edges of MTP and aniline modified QDs move about 0.2 eV towards the lower energy direction. Through this study, we can see that the energy level position of QDs depends largely on their surface ligands indicating that the energy level can be adjusted by ligand exchange, which is of great significance for the research of photocell or LED and other fields.^[4,144,145]

As a member of narrow band gap semiconductor III–V family, InSb is an important modern semiconductor industrial

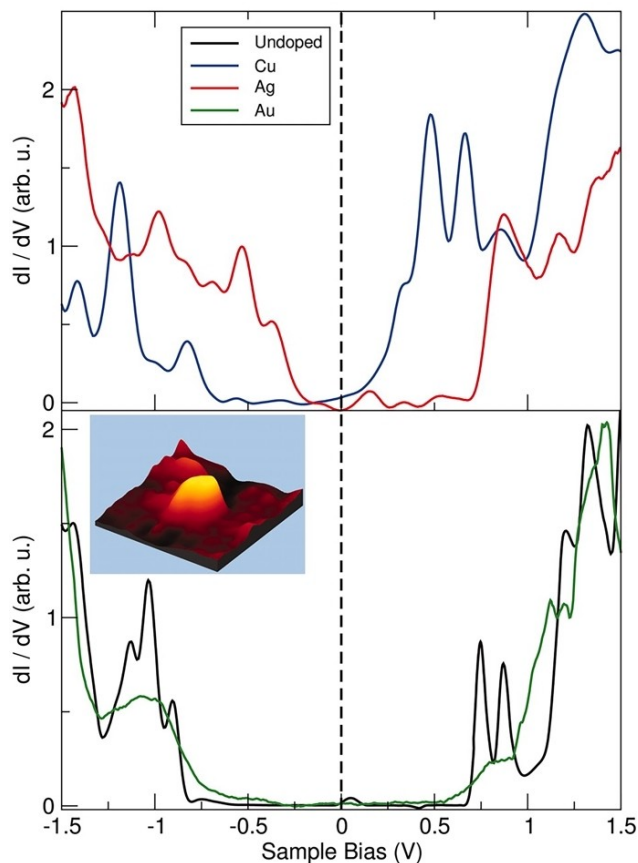


Figure 8. The effect of doping on the STM tunneling spectra. Four dI/dV versus V tunneling spectra at 4.2 K of undoped (black trace), Au-doped (green trace), Cu-doped (blue trace), and Ag-doped (red trace) InAs nanocrystals, nominally 4 nm in diameter. The inset shows an STM image of a single (Ag-doped) QD on which STS data were measured.^[134] These figures are taken from Ref. [134] with permission.

material.^[146,147] Wang et al.^[148] studied the electronic structure of InSb QDs with a diameter of 3–7 nm. InSb QDs show a strong quantum confinement effect. When the size of the QDs is reduced, the energy gap between the band gap and the conductive-valence band energy level will increase rapidly. At the same time, they also carried out similar experiments on InAs QDs, another member of the III–V semiconductor. The difference of tunneling spectra indicates the difference of tunneling process. Theoretical calculations strongly suggest that the electron tunneling of InSb QDs occurs through quantum confined levels connected with L-points of Brillouin zone, which is the first time to observe this kind of tunneling process in colloidal III–V QDs.

4.1.2. Energy Level Structure of Colloidal InAs QDs in Two-Dimensional Array

The ligands on the surface of colloidal QDs enable them to be stably dispersed in non-polar organic solvents. Large area of QD arrays, i. e., nanocrystalline superlattices or QD solids, can be achieved by self-assembly on a flat substrate surface through drop coating or spin coating.^[4,149–151] The physical properties of the nano-superlattice depend on the nature, shape, and size of the nanocrystalline units, as well as the electronic coupling between the units, etc. These factors determine the energy level distribution and the size of the band gap of the QDs. As a result, nanocrystalline superlattices have broad application prospects in optoelectronics, thermoelectricity, magnetic applications, spintronics, and catalysis.^[150] In previous studies, the electronic coupling between the dots in the QD array has always been a major concern.^[152] Steiner et al.^[35] carried out STS measurements on two-dimensional InAs arrays which showed short-range order and found that the main factors affecting the size of the band gap and the electronic state in the QD array were the distance between the nearest neighbors and the corresponding coordination number. As shown in Figure 10(c), compared with isolated QDs, the band gap of InAs QDs in the array is significantly reduced, which is due to the coupling between the electronic wave functions of adjacent QDs. Compared with the edge dots, the internal dots have more adjacent QDs, and the change is more obvious on the internal QDs. Figure 10(d) shows the STS results of QDs in other regions. Compared with Figure 10(c), the valence band redshift is more obvious, but it is still less than the conduction band redshift, and the band gap decreases more, indicating a stronger coupling phenomenon between local QDs. Besides, they also found a steplike structure at the conduction band of the tunneling spectra. As shown in Figure 10(e), the discrete energy level structure of QD is masked. This steplike structure generally appears in the very dense and ordered two-dimensional array tunneling spectrum, which is formed by the superposition of minibands with constant density of states. From the STM image in Figure 10(a), it is obvious that the density of the sample array in the experiment is high, and the probability of observing the steplike structure in the tunneling spectra is low. Possibly, these steplike structures are associated with collective levels spanning a few strongly coupled QDs and can be viewed as precursors of the formation of minibands. Collective minibands can develop also in assemblies that do not exhibit long-range order.

4.1.3. Wavefunction Mapping of InP Semiconductor Nanocrystals

Using the ultra-high spatial and energy resolution of STM/STS, Maruccio et al.^[153] positioned the STM tip on a single

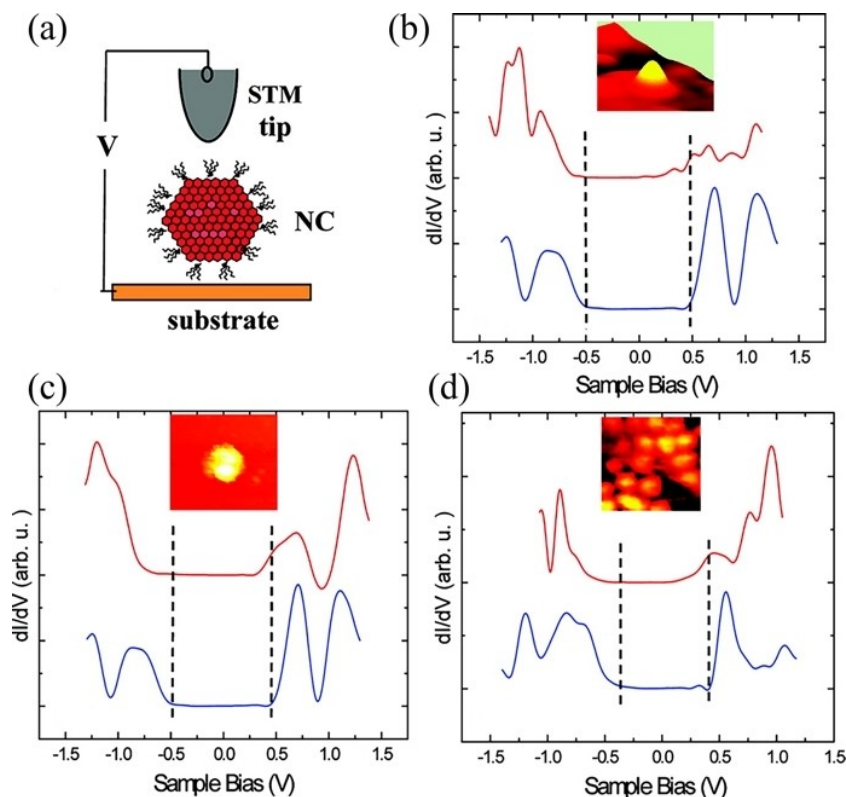


Figure 9. (a) Schematic of the STS measurement configuration. (b–d) Tunneling (dI/dV vs V) spectra of (b) a single aniline-capped InAs QD (top curve) in comparison with a single TOP-InAs QD (bottom curve), (c) a single MTP-modified InAs QD (top) in comparison with a single TOP-capped InAs QD (bottom) and (d) an aggregate of MTP-modified InAs QDs (top) in comparison to an aggregate of TOP-InAs QDs (bottom).^[143] These figures are taken from Ref. [143] with permission.

InP QD. Under a certain bias voltage and current, the distance between the tip and the QDs was stabilized for wave function imaging experiments. Under the condition of “shell-tunneling”, dI/dV can approximately reflect the LDOS of the QD. For this reason, the measured dI/dV signal corresponds to the square of the wavefunction at this energy, so it can realize the distinction between the wavefunctions of the S and P states in a single InP QD, and then realize the study of the influence of the coupling of the surrounding QD and the Au substrate on the electronic wavefunction of the target QD. In the experiment, they selected three QDs of similar size for measurement, and the results are shown in Figure 11. When it resonates with the S state, it can be observed that the intensity distribution is approximately circular and symmetrical as shown in Figure 11(b). With the increase of bias voltage, tunneling resonates with the P-state. At this time, two clear P-like lobes in Figure 11(b) can be observed, with an obvious node in the middle. However, the hybridization between P_x and P_y states was not observed in the experiment. The reduction of the degeneracy of the P state can be explained by several different mechanisms: the change of the shape of the QD, the existence

of the piezoelectric field and the coupling with the substrate.^[60,154,155] The measurement results of STM and TEM (Transmission Electron Microscope) show that the shape of QDs has not changed, and no strain has occurred, so it cannot be caused by piezoelectric effect. Thus, Maruccio et al. believe that the coupling of QDs and Au(111) substrate is the reason for the reduction of P-state degeneracy. Due to the need high bias voltage, and the tunneling junction is difficult to exist stably under a high bias voltage, the experiment has not been able to obtain a clear image of a higher energy state (such as the D state or the P state perpendicular to the surface).

4.2. CdSe Quantum Dots

4.2.1. Energy Level Structure of Single Colloidal CdSe QDs

In 1999, Alperson et al.^[59] obtained the tunneling spectra of CdSe QDs and observed the atom-like electronic states and size-dependent relationship. The results are shown in Figure 12. The band gap value of QD can be obtained from the STS spectrum, and the band gap increases with the decrease of

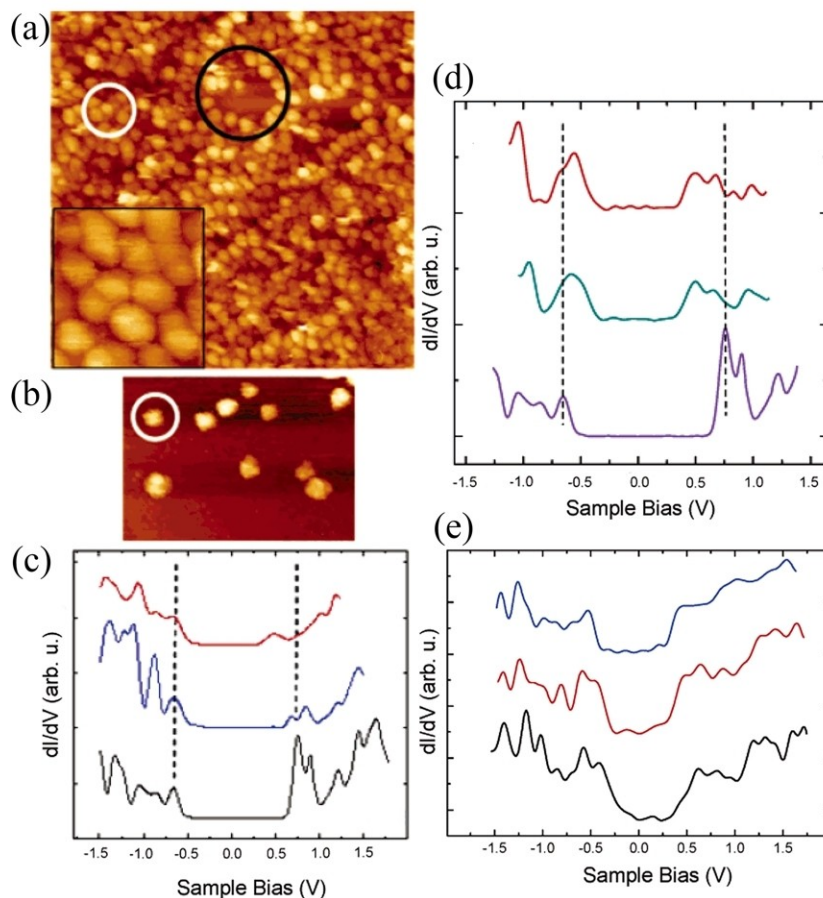


Figure 10. (a) STM image of array composed of InAs QDs at 4.2 nm. (b) STM image of isolated QDs, with a diameter of 4.2 nm. (c) Three tunneling spectra acquired on QDs at different locations: the black curve on an isolated dot shown in (b), the blue curve on a QD located at the edge of the void marked by the black circle in (a) and the top red curve on a QD located within the assembly, inside the white circle in (a). (d) Tunneling spectra of QDs in the other region: the above two curves are QDs in the array, and the conduction band and valence band are redshifted relative to the tunneling spectrum measured on the isolated QD. (e) The tunneling spectra of steplike structure appears at the conduction band, and the trace of the superposition of discrete energy levels at the steplike can be clearly seen in the lower two curves.^[151] These figures are taken from Ref. [35] with permission.

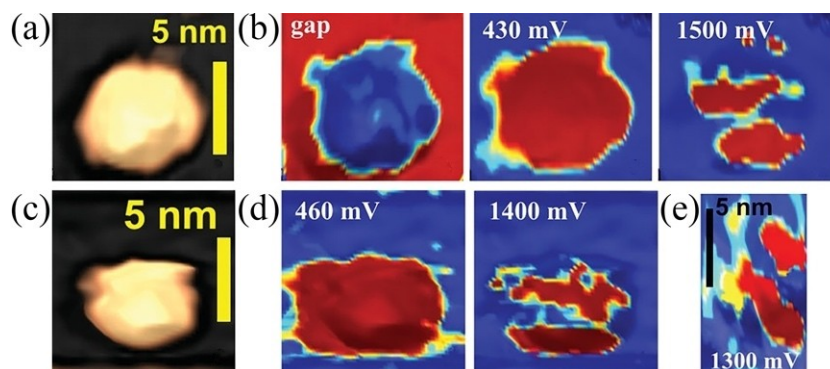


Figure 11. (a) Topography. (b) simultaneously acquired STS maps of a single representative nanocrystal, taken in the bandgap and at 430 and 1500 mV, respectively. (c) Topography and (d) STS maps showing the S and P states of another nanocrystal. (e) A P state with a different orientation from a third nanocrystal.^[153] These figures are taken from Ref. [153] with permission.

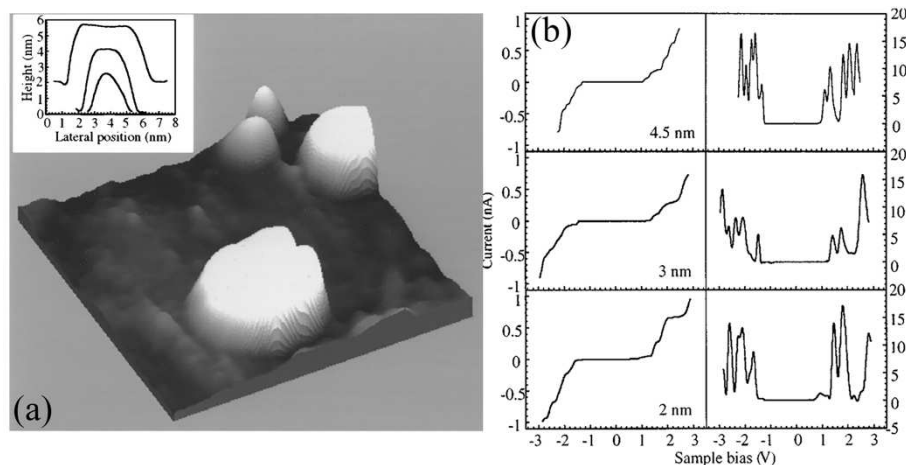


Figure 12. (a) STM topography image ($12 \times 12 \text{ nm}^2$) showing four CdSe QDs electrodeposited on Au. (b) Tunneling current-voltage spectra acquired at 4.2 K on the three QDs in (a) and corresponding conductance spectra obtained numerically from the I–V curves.^[59] These figures are taken from Ref. [59] with permission.

QD size. The double peak observed at the position of about 1.2 V at positive bias voltage corresponds to the S_c orbital of the QD, and the peak at higher bias is the result of the resonance of the P_c orbital. The results at negative bias voltage are a series of resonance peaks reflecting the hole energy levels in the valence band. The double and multiple peaks observed in STS indicate that the degeneracy of energy levels is destroyed under the Coulomb effect.

Then Vanmaekelberg group^[57,121] used the “shell-tunneling” and “shell-filling” spectrum to further study the 4.30.4 nm single spherical CdSe QDs. The “shell-tunneling” spectrum showed the quasi-particle band gap and the first five electronic energy levels of CdSe QDs. The results were in good agreement with the single-electron energy level spectrum calculated by the pseudopotential theory. According to the order of energy increase, the five peaks correspond to the tunneling of s, p, d, s' and f-type electronic orbitals in CdSe QDs. Under the condition of “shell-filling”, because of the influence of the Coulomb interaction between the additional electrons in the QD, the tunneling spectrum becomes more complex, and the Coulomb repulsion energy can also be calculated using the pseudopotential of the interaction between the multi-body electrons.

4.2.2. Electron-Phonon Interaction in CdSe Quantum Dots (Rods)

The coupling of electrons and lattice vibration is the key to understand the photoelectric characteristics of semiconductors. However, in bulk semiconductor materials, this coupling is quite weak owing to the delocalization of the electron and hole wave functions. In semiconductor QDs, the coupling is

expected to be greatly enhanced due to the strong restriction of the electron and hole wave functions. STS provides a unique method for studying the coupling between single electron (hole) and lattice phonon.

In 2008, Jdira et al.^[156] analyzed the reasons for the broadening of the S_c state in the STS of CdSe QDs. Figure 13(a–b) shows the single CdSe QD tunneling spectrum with diameters of 3 nm and 5 nm respectively. Compared with the slight asymmetry of the S_c state of the 5 nm QD, the S_c state of the 3 nm QD has better symmetry, and full widths at half maximum (FWHM) increases with the decrease of the size of the QD. When studying the effect of the set point current on the tunneling resonance broadening, the FWHM of the S_c state has little change when the set point current is increased and kept under the “shell-tunneling” condition. The FWHM of the S_c state of the tunneling spectrum obtained at different temperatures is normalized. It is found that the FWHM increases linearly with the increase of ambient temperature in the temperature range of 5–300 K. The thermal energy generated by changing the set point current at low temperature is far less than the longitudinal optical phonon energy, so the broadening caused by temperature can be ignored. The shape of the S_c state mainly depends on the electron-phonon coupling strength. Small-sized QDs have stronger electronic constraints, so the electron-phonon coupling is also stronger, so the S_c state presents better symmetry. The theoretical calculation also shows that the Gaussian fitting of the electron-phonon coupling is consistent with the tunneling spectrum. The line shape of the tunneling spectrum is given by a series of peaks, and its amplitude is determined by the coupling strength of the electron and phonon. Accordingly, the coupling of the longitudinal optical phonon

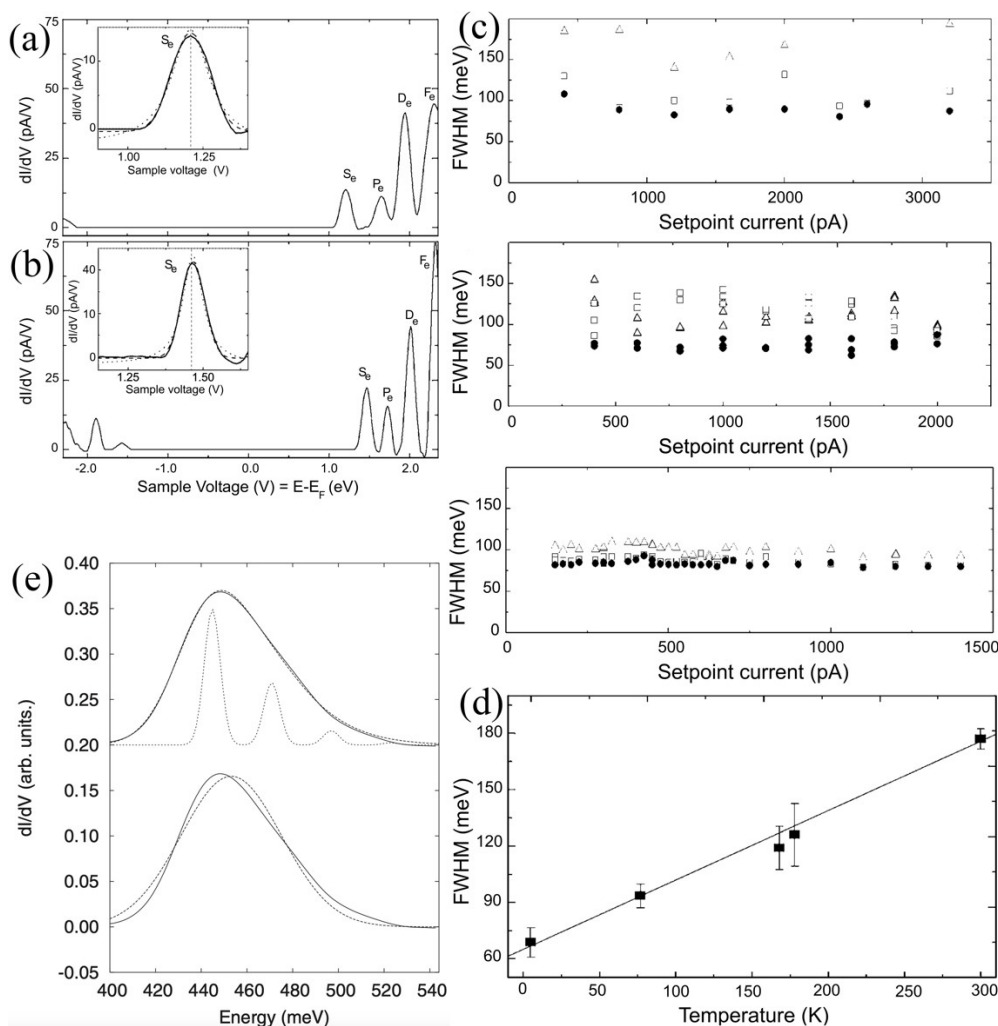


Figure 13. Differential conductance spectra for isolated CdSe QDs in the shell-tunneling regime for two samples with TEM, which determined core sizes of (a) 3.0 and (b) 5.0 nm. (c) FWHM of the S_e (●), P_e (□), and D_e (△) peaks, which are measured as a function of the set point tunneling current. (d) FWHM of the S_e peak, which is measured on CdSe dots, with a TEM determined core size of 6.1 nm, as a function of temperature. (e) Comparison between experimental (continuous line) and calculated (dotted lines) differential conductances for an electron in a S_e state of a CdSe QD, with a diameter of 6.1 nm.^[156] These figures are taken from Ref. [156] with permission.

and the tunneling electron is the main reason for the broadening of the S_e state in the tunneling spectrum.

Sun et al.^[118] studied the STS of CdSe spherical and rod-like colloidal QDs using low-temperature STM, and quantitatively illustrated the electron-phonon coupling strength. They carried out STS measurements on the mixture of spherical (diameter 3 and 6 nm) and rod-shaped (diameter 3.5 nm, aspect ratio between 1 and 4) colloidal CdSe QDs. Figure 14(b) shows the tunneling spectrum of spherical CdSe QDs with diameter of 6 nm and rod-shaped QDs with diameter of 3.5 nm (aspect ratio of about 2). When the electron and phonon are coupled, the S state in the STS includes a ground state and several vibrational excited states, separated by phonon energy. In the case of phonon mode, the

calculated tunneling spectrum is basically consistent with the experiment. Compared with the QDs located in the array, the electron-phonon coupling strength of the isolated QDs is smaller, but the phonon energy that determines the vibration peak interval itself is constant. Figure 14(c) shows the distribution of the spacing of the phonon replica. It is not difficult to find that the most samples are distributed around 31 mV. According to the potential distribution of the “tip-QD-substrate” junction, the conversion of the peak interval into the energy interval (26 meV) is very consistent with the known optical phonon energy of the bulk CdSe.

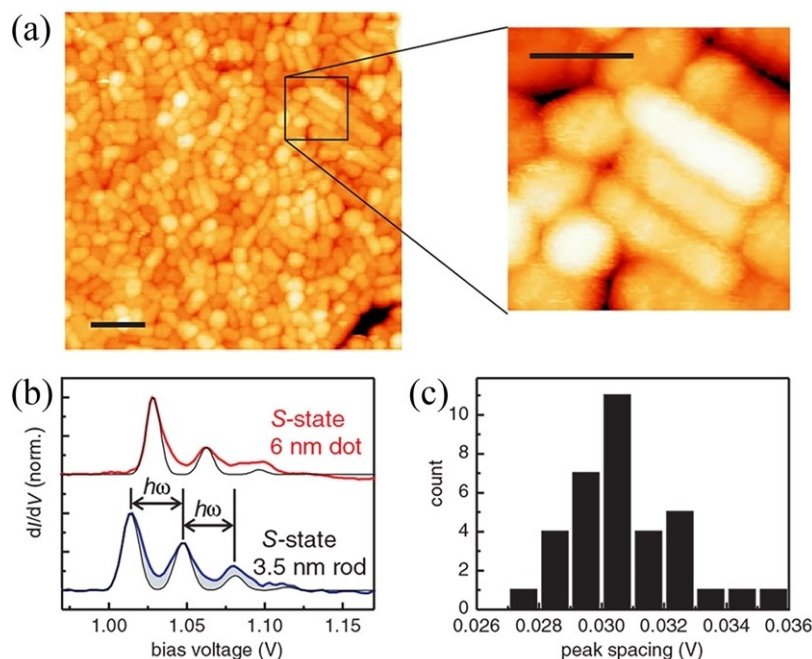


Figure 14. (a) STM topography of arrays of colloidal CdSe QDs on a HOPG substrate. Analysis of the e-ph coupling strength. (b) Experimental data for 6 nm spherical dot and 3.5 nm diameter nanorod along with the fits to a theory. (c) Distribution of the spacing of the phonon replica.^[118] These figures are taken from Ref. [118] with permission.

4.3. PbX (X=Se, S, Te) Quantum Dots

4.3.1. PbX QDs Absorption Peak

PbX (X=Se, S, Te) has rock salt crystal structure, and its basic band gap is located at four L-points in the Brillouin zone, so its carrier wave function is strongly restricted. The HOMO and LUMO of its QDs become eightfold degenerate. Compared with the energy levels of II–VI and III–V QDs, the multiplicity of other discrete energy levels is also four times higher PbX (X=Se, S, Te).^[157–161] Because the electron, hole, and Bohr radius of PbS are much larger than that of CdSe, it is easier to obtain the strongly confined region of the electron and hole, so PbX QDs are very suitable for the study of the strongly dimensional confined properties. The nonlinear optical properties of semiconductor QDs are expected to be greatly improved in the strongly restricted region, so PbX QDs have potential application value in nonlinear optics.^[158] Theoretical calculation predicts that there are nearly mirror symmetric electronic states in the conduction and valence bands of PbX QDs,^[158] so the optical transition between single-photon bands should follow the parity selection rule, that is, only the transitions in the same symmetric state (S_h-S_e , P_h-P_e) are allowed. However, this theoretical prediction is contrary to the results of optical absorption measurement.^[162–165] In the experiment, asymmetric transitions, i. e., strong spectral peaks of $1S_h-1P_e$ and $1P_h-1S_e$, were

observed. This inconsistency has triggered a long and fierce debate on the interpretation of various absorption characteristics in PbSe and PbS QD samples.^[166,167]

The study shows that there are many peaks in the absorption spectrum of PbSe QDs, and the first peak corresponds to the S_h-S_e transition with the lowest energy. However, different interpretations appear in the analysis of the second peak. First, its energy is lower than the calculated P_h-P_e transition energy. Therefore, some people propose that the second absorption peak is generated by the S_h-P_e transition,^[159,165] but some studies believe that the intensity of the transition should be ignored¹⁵². In 2005, Vanmaekelberg group^[157] obtained the STS of PbSe spherical QDs under the condition of “shell-tunneling”. The single-particle band gap is consistent with the value calculated by optical measurement and tight-binding theory. The optical absorption spectrum of PbSe in Figure 15(e) shows that the second exciton transition is equivalent to the P_e-P_h energy measured by STM. As shown in Figure 15(f), the S_e-P_h and P_e-S_h obtained from the tunneling spectrum are significantly lower than the optical transition energy. Hence, it is confirmed that the second exciton resonance is not the S–P transition but the P_e-P_h transition. In 2008, Rolf et al. remeasured the optical properties of PbSe QDs in detail and obtained almost the same results as above,^[168] which fully proved the powerful function of STM in analyzing colloidal QDs.

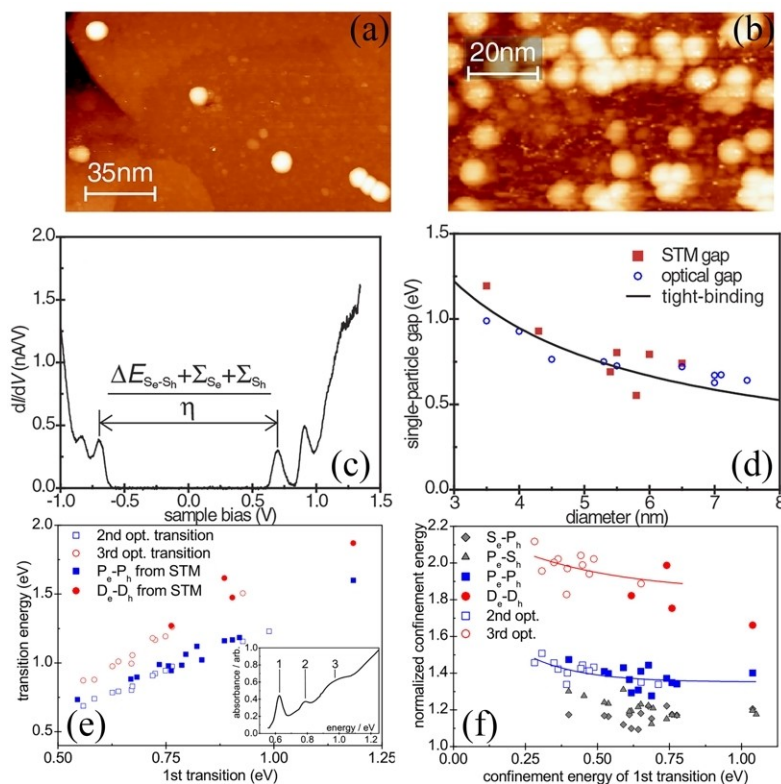


Figure 15. Large scale scans of 5.3 nm (a) and 4 nm (b) PbSe nanocrystals covalently bound to an Au substrate. (c) Example of a measured tunneling spectrum (dI/dV , V) on an isolated PbSe nanocrystal. (d) Comparison of the single-particle HOMO-LUMO gap measured by STM (filled squares), the optical gap (open circles)^[164,169] and the single-particle gap from TB calculations (solid line).^[170] (e–f) Comparison between the observed optical transitions and the energy levels measured by STS.^[157] These figures are taken from Ref. [157] with permission.

PbS QDs have more isotropic bands and almost identical electron and hole effective masses that make them more suitable for separating the effects due to anisotropy from those due to breakdown of parity conservation. Diaconescu et al.^[166] found that the second optical transition was closer to the asymmetric $1S_c-1P_h$ and $1P_c-1S_h$ transitions than the symmetric $1P_c-1P_h$ transitions (as shown in Figure 16b) by comparing the STS measurements and optical measurements of single PbS QDs of different sizes.^[162] Moreover, the position of the third optical transition is very consistent with that of the symmetric $1P_c-1P_h$ transition, while the position of the fourth optical transition is very close to that of the asymmetric $1D_c-1P_h$ and $1P_c-1D_h$ transitions, which indicates that the electronic transition in PbS QDs does not strictly follow the parity selection rule, so it can show strong optical absorption characteristics.

4.3.2. The Linewidth of the Resonances of Individual PbSe Nanocrystal

Overgaag et al.^[171] acquired the STS of single PbSe QDs with different sizes and found the phenomenon of energy level

broadening. They focused on the energy level broadening of the first resonance e_1 and h_1 corresponding to the lowest electron and hole orbits. The data in Figure 17(a) is fitted with Gaussian function. The results are shown in Figure 17(b). The FWHM of e_1 and h_1 increases with the decrease of the size of QDs, and the slope of change has an obvious jump at about 5 nm in diameter. The coupling of electrons and phonons in nanostructures is an important source of energy level broadening in transport, but Overgaag et al. believed that this could not fully explain the phenomenon that the energy level broadening significantly increased with the decrease of QD size observed in the experiment. Moreover, it is proposed to add the intervalley coupling into the tight-binding calculation. The functional relationship between the electronic structure and the diameter of PbSe QDs obtained shows that the splitting degree of S_c and S_h energy bands increases significantly with the decrease of the size of QDs. This study shows that the energy level broadening is mainly caused by the electron-phonon coupling and valley coupling between different L-points in the Brillouin region, which successfully explains the above experimental observations. The combination of theoretical and experimental results further shows that

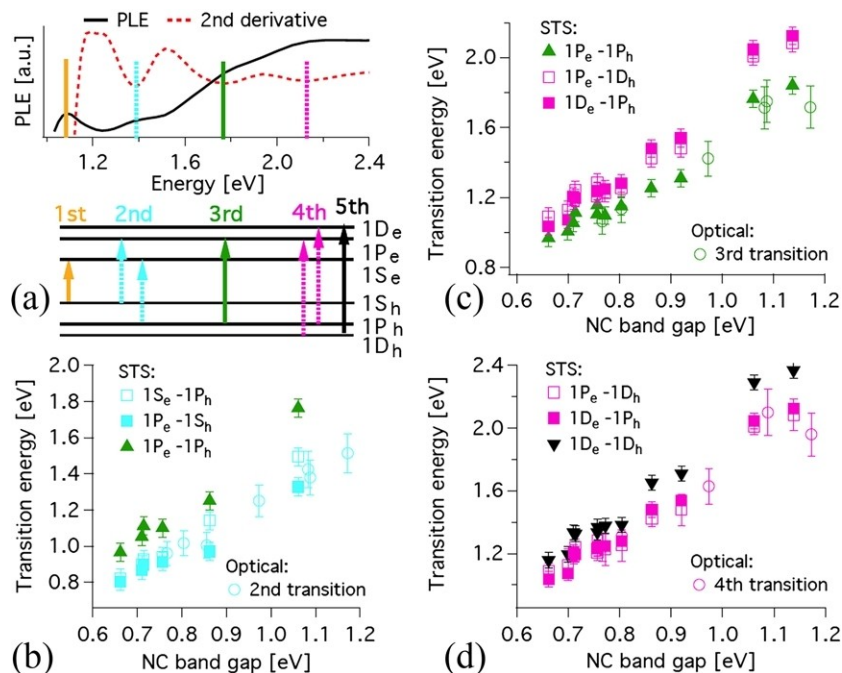


Figure 16. (a) The first four optical transitions observed in the PLE spectrum (solid line) and its second derivative (dashed line) of the sample. (b–d) The comparison of energies of various symmetric and asymmetric interband transitions derived from the STS measurements (squares and triangles) and optical transitions (circles) from the PLE and single-photon absorption spectra^[166] (optical data are from reference^[162]). These figures are taken from Ref. [166] with permission.

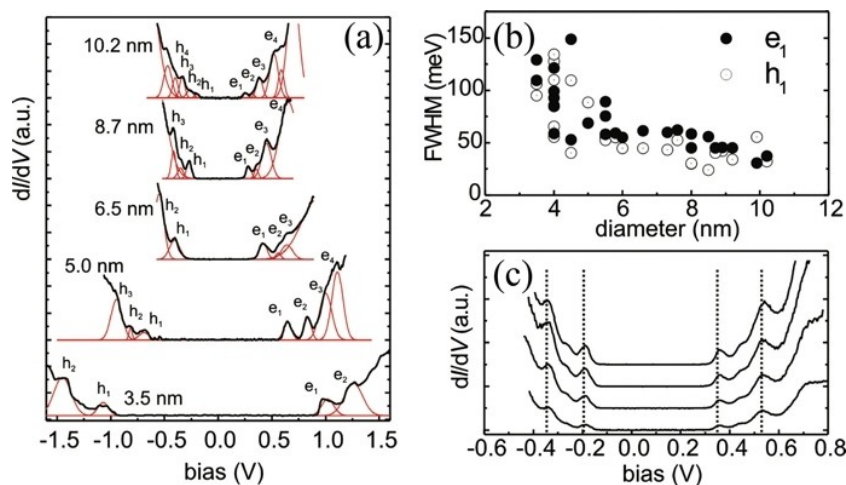


Figure 17. (a) Energy-level spectra obtained above PbSe nanocrystals of different sizes. (b) FWHM of the first electron (hole) resonance vs the size of the PbSe QDs. (c) Spectroscopy measurements with different tunneling current set-points.^[171] These figures are taken from Ref. [171] with permission.

for QDs with diameter less than 5 nm, the latter plays a dominant role.

4.3.3. PbSe Nanocrystals in Array

Because the effective mass of electrons and holes in PbSe QDs is very low, PbSe QD superlattices are excellent candidates for observing quantum mechanical coupling. Liljeroth et al.^[60] studied the LDOS of PbSe QD arrays by low temperature STM and STS. From the comparison between the tunneling

spectrum of QDs in the array in Figure 18(c) and isolated QDs, it can be found that the PbSe QD array has inter-point coupling phenomenon. At the same time, two coupling phenomena are found in the comparison between the three different regions of the array and the isolated QD. One is the significant broadening of the conduction band energy level, and the coupling strength (defined as the additional broadening of DOS characteristics) is 50–150 meV, as shown in Figure 18(d); The other is the obvious steplike shape at the conduction and valence band, as shown in Figure 18(e), indicating that the electronic and hole orbits of the adjacent PbSe QDs have a strong quantum coupling phenomenon. This band selective coupling is of great guiding significance for the design of QD materials with specific properties.

In addition to the research on the array composed of unary QDs, Overgaag and Liljeroth et al.^[34] also carried out STM and STS research on the array composed of PbSe QDs and CdSe QDs, as shown in Figure 19. They prepared PbSe QD monomers and dimers dispersed in CdSe QD matrix. CdSe QDs array can be regarded as an inert matrix with PbSe QDs stably dispersed. The results show that the STS of single PbSe QDs in CdSe matrix is almost the same as that of isolated PbSe QDs fixed on the substrate by chemical method. In the study of small and medium-sized PbSe QD aggregates in dispersed CdSe matrix, it was found that there were different degrees of electron delocalization in small aggregates with coupling strength of 10–20 meV. Their results show the feasibility of quantitative research on arrays with different structures and provide an important reference for further research on ordered binary QD solid systems.

As shown in Figure 20(a), recently Notot et al.^[61] peeled the lead oleate ligand from the PbSe QD {100} facets to realize the epitaxial connection of QDs, forming a p-type-doped superlattice with a square geometry, where the unbound facets are still passivated with oleate ligands. The STS shows that the occupied energy level of the QDs in the superlattice is affected by the neighboring QDs and shows the electronic coupling of the valence band state, as shown in Figure 20(c). Besides, as shown in Figure 20(d), they also found that new states appear in the band gap of the original monomer in a few QDs. The analysis of this phenomenon shows that it is caused by the unpassivated sites on the (111) facets, because these QDs with defects are randomly distributed in the superlattice, which can capture electrons and release many free holes. They act as electron acceptor QDs in the host QD lattice, mimicking the role of dopant atoms in a semiconductor crystal.

4.3.4. Surface Study of PbS QDs

The performance of colloidal QD photovoltaic devices is strongly affected by the local sub-bandgap state related to surface passivation or defects. The nature of the surface state of QDs can be understood by analyzing the influence of defect structure on its properties at the atomic scale.^[172] Kislitsyn et al.^[62] studied various electronic states of ligand-free PbS QDs after annealing using STS and carried out dI/dV mapping of the sub-band gap state of a single PbS QD, as shown in Figure 21. The sub-bandgap state diagram clearly shows the LDOS of the non-stoichiometric adsorption atoms self-assembled on the surface of QDs. The atomic-scale spatial

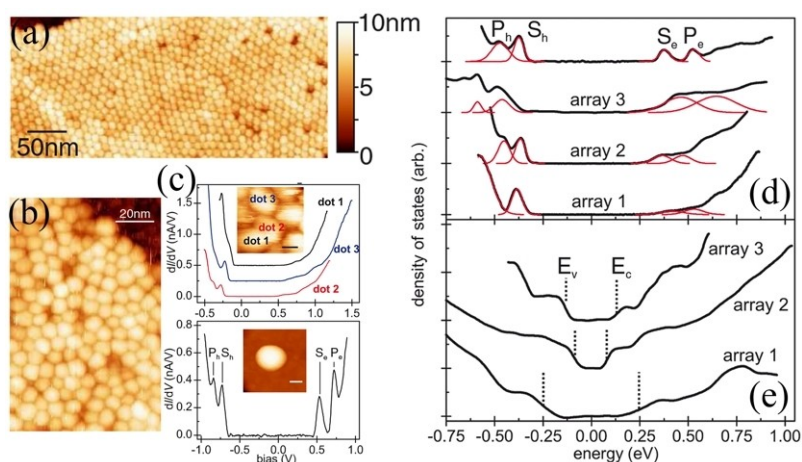


Figure 18. (a) Typical large-scale STM topography of 7.3 nm diameter PbSe QDs (array 1). (b) Large-scale topographic image of 5.3 nm diameter PbSe QDs (array 2). (c) Experimental dI/dV spectra measured on the three neighboring QDs (top) and spectrum of an isolated PbSe QD (5.3 nm diameter) linked to Au (111) using hexanedithiol (bottom). (d) Prototypical LDOS measured on PbSe QD sites in an array. The spectra were measured on three different samples, 7.3 nm diameter QDs (array 1), 5.3 nm QDs (array 2), and 5.3 nm QDs with an additional octanethiol self-assembled monolayer in between the PbSe QDs and the gold substrate (array 3). (e) Examples of spectra in the full coupling regime. Spectra were measured on the same samples as in (d).^[60] These figures are taken from Ref. [60] with permission.

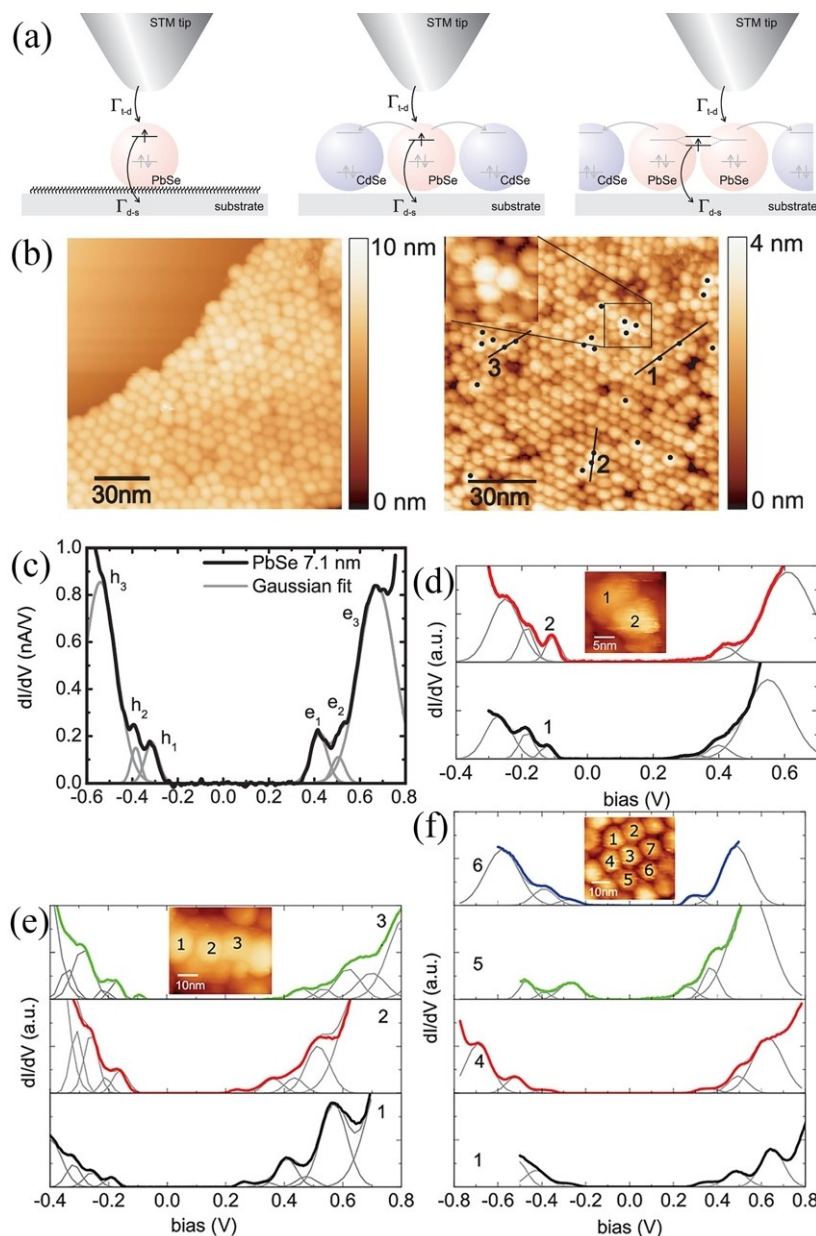


Figure 19. (a) Schematic of the tunneling processes (denoted by arrows) that are possible with isolated PbSe QDs and QDs embedded in a matrix of CdSe QDs: (left) a single PbSe QD chemically linked to the substrate with hexanedithiol; (center) an isolated PbSe QD surrounded by CdSe QDs, in which the incoming electron can tunnel either directly or via neighboring CdSe QDs to the substrate; (right) the electronic levels in a PbSe QD dimer can be strongly coupled and the electron can delocalize over the two QDs. (b) Topographic and spectroscopic identification of PbSe QDs in a CdSe QD matrix: (left) large scale STM image of a hexagonally packed monolayer of CdSe QDs with an average diameter of 6.1 nm; (right) STM image of 7.1 nm PbSe QDs (marked with black circles) dispersed in a matrix of 6.1 nm CdSe QDs. (c) Spectroscopy on individual PbSe QDs with diameters of 7.1 nm embedded in a CdSe QD matrix. (d) Spectroscopy on a 9.8 nm PbSe dimer embedded in a CdSe matrix. (e) Spectra measured on three QDs on a chain of four 9.8 nm diameter PbSe QDs—the thin solid lines represent Gaussian distributions fitted to the resonances. (f) Representative spectra on QDs that are part of a larger aggregate of 9.8 nm diameter PbSe QDs.^[34] These figures are taken from Ref. [34] with permission.

structure of these sub-bandgap states will have a great impact on the photophysical properties of such QDs. The dI/dV mapping of STS can effectively identify the electronic state changes of the surface defects and impurities of QDs.

Gervasi et al.^[63] also used STS to study the sub-bandgap state in a single ligand-free PbS nanocrystals in real space. Their STS spectra show that surface reconstruction leads to the formation of sub-bandgap electronic states. The nature of

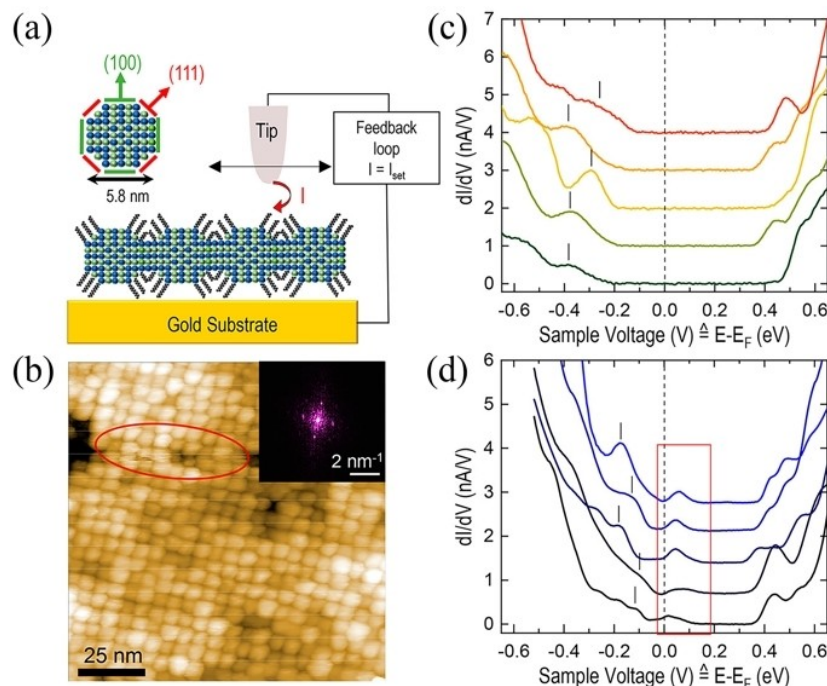


Figure 20. (a) Facet orientations of a PbSe QD and simplified schematic of the epitaxially connected PbSe QDs characterized with STM. (b) STM image of a superlattice showing the close packing of PbSe QDs in a square superlattice. The red oval encircles fuzzy QDs highlighting a strong interaction of the ligands with the STM tip. (c) Examples of tunneling spectra acquired on five different individual QDs, where a zero-conductance region is clearly measured on both sides of the zero bias. (d) Examples of tunneling spectra acquired on five different individual QDs showing in-gap states at low positive bias, in the region delineated by the red rectangle.^[61] These figures are taken from Ref. [61] with permission.

surface reconstruction varies with the change of surface stoichiometric ratio. The lead rich surface produces unoccupied sub-bandgap states, and the sulfur rich surface produces occupied sub-bandgap states. The region with high non-stoichiometric ratio will produce occupied and unoccupied states at the same time, showing obvious band gap reduction.

Ueda et al.^[64] measured the LDOS on the surface of PbSe QD superlattice in ultra-high vacuum using a low-temperature STM. As shown in Figure 22 (a), they obtained the relationship between the LDOS of QDs and the dose of trimethyl aluminum (TMA). The results showed that the band gap of the QDs after TMA treatment increased significantly. The relationship between the band gap and TMA dose in Figure 22(b) shows that the band gap increases with the increase of TMA dose, when the dose is $\sim 5 \times 10^6$ L, it is close to the value of optical band gap. Their results confirmed that adding TMA vapor in vacuum can passivate the surface state, improve the STM imaging quality, expand the band gap, and improve the charge transfer and transistor performance, providing important information for the possible application of PbSe QD film in future optoelectronic devices.

4.4. Core/Shell Structure Nanocrystals

Colloidal QDs with core/shell structure refer to the structure that a layer of shell material different from nuclear QDs is grown on the surface of QDs to form an outer layer of material to wrap the inner core. Compared with traditional QDs, it shows excellent performance, including improved fluorescence efficiency and significantly improved stability. Therefore, QDs with core/shell structure have broad application prospects in solar cells, biological fluorescence labeling, etc..^[67,173,174]

Colloidal QDs with core/shell structure have more complex electrical properties than single QDs. As shown in Figure 23, there are three main energy level arrangement relationships. The shell material of Type I QDs has higher conduction band energy level and lower valence band energy level than the core material, forming an embedded energy band structure. Both electrons and holes are confined in the core (left of Figure 23a). CdSe/ZnS QDs represent the most common form of Type I heterostructure. On the contrary, the anti-I material is an “inverted” structure with electrons and holes confined to the shell. Type-II heterostructures tend to be composed of materials with medium band gap (> 1.3 eV).^[69] According to its characteristics, the conduction band and

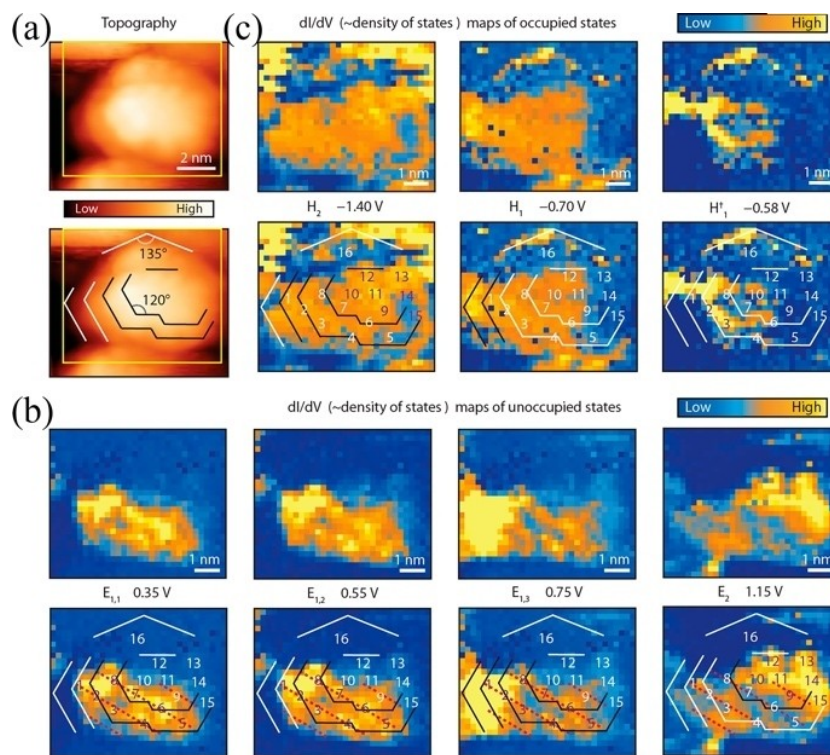


Figure 21. (a) Topographic images of nanocrystal. Bottom image is marked to indicate step edges with 120° angles oriented along (110) directions; the same set of marks is used in the bottom images of panels b and c for reference. (b) DOS maps for unoccupied states of nanocrystal measured at the indicated bias voltages. The state $E_{1,n}$ is mainly concentrated in the left and bottom of the QD, and near the step observed in the STM topography. The empty state E_2 is delocalized in the entire QD, and mainly concentrated in the upper right part of the QD (position 10–15 in (b)). There are no obvious steps. (c) DOS maps for occupied states of nanocrystal measured at the indicated bias voltages.^[62] These figures are taken from Ref. [62] with permission.

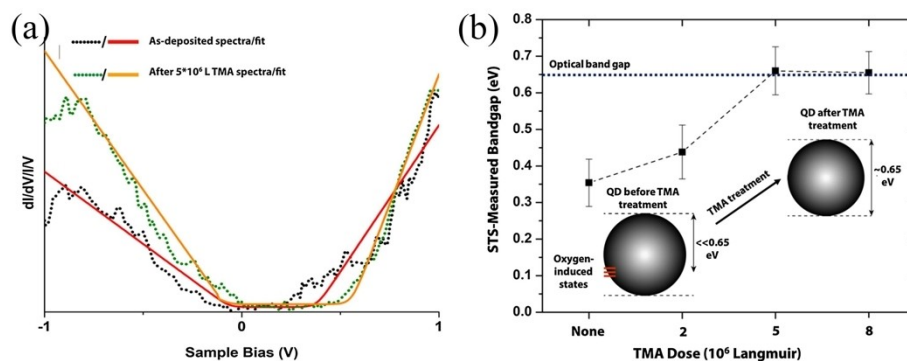


Figure 22. Effect of TMA dosing on QD band gap. (a) Representative ST spectra (dashed lines) and fits (solid lines) for a PbSe QD before (red) and after (orange) a 5×10^6 L dose of TMA. (b) Before TMA dosing, the STS-measured band gap of QDs in monolayer superlattices is only 0.35 ± 0.07 eV, much smaller than the optical band gap of the QD films (~ 0.65 eV). The band gap increases with increasing TMA dose until it saturates at 0.65 ± 0.06 eV, close to the value of the optical band gap.^[64] These figures are taken from Ref. [64] with permission.

valence band of one material are higher than that of the other material (Figure 23b), and the moderate band gap is easier to achieve this energy level arrangement. Most importantly, this energy level structure is that the two excited carriers are transported to two separate regions respectively. Specifically,

electrons will be confined in materials with lower conduction band (whether core or shell), while holes will be in materials with higher valence band, thus achieving effective separation of carriers. Another important structure is that one kind of carrier is limited in a single material, while the other kind of carrier is

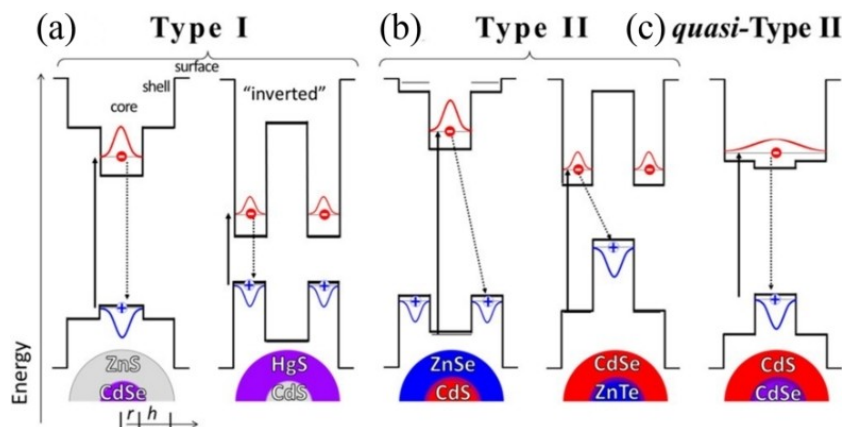


Figure 23. (a) Type-I QDs feature a nested alignment, causing both the electron and hole to reside principally in either the core (left) or the shell (right). (b) In Type-II QDs, a staggered alignment of conduction and valence bands pulls band-edge electrons and holes into separate parts of the core/shell QD. (c) In quasi-type-II QDs, one carrier remains localized in a single component of the heterostructure (here, the hole), while the other is largely delocalized throughout the entire QD.^[69] These figures are taken from Ref. [69] with permission.

completely delocalized between multiple materials, namely, quasi-II heterojunction. The conduction band of the shell material of the quasi-Type-II QD is like the edge of the nuclear QD, and the valence band shifts obviously.

4.4.1. Core/Shell QDs

In 2001, Millo et al.^[58] studied the effect of ZnSe shell on the electrical properties of InAs QDs. As shown in Figure 24, by comparing the core/shell QD tunneling spectra of the InAs core with a radius of 1.7 nm and the 2 and 6 layers of ZnSe shell, they found the multimodal structure corresponding to the S_c state and the P_c state. With the increase of the shell thickness, the band gap of the core/shell QD remains

unchanged, but the energy level gap between S_c and P_c decreases significantly. Besides, the measured S_c state of STM in real space is limited to the core region of InAs, while the P_c state extends to the ZnSe shell, which reduces the quantum confinement effect. Accordingly, with the increase of shell thickness, the energy of P_c energy level decreases and the S_c state level does not move, which is consistent with the wave function image calculated by using the spherical model.

Grimbom et al.^[65] studied the effect of PbS shell on PbSe QDs by STS. The radius of PbSe nucleus is 1.5 nm, and the thickness of PbS shell is 0.75–2.5 nm. The experimental results show that with the increase of the shell thickness, the band gap decreases, accompanied by the decrease of the high-energy inter-band transition. This result is the same as the

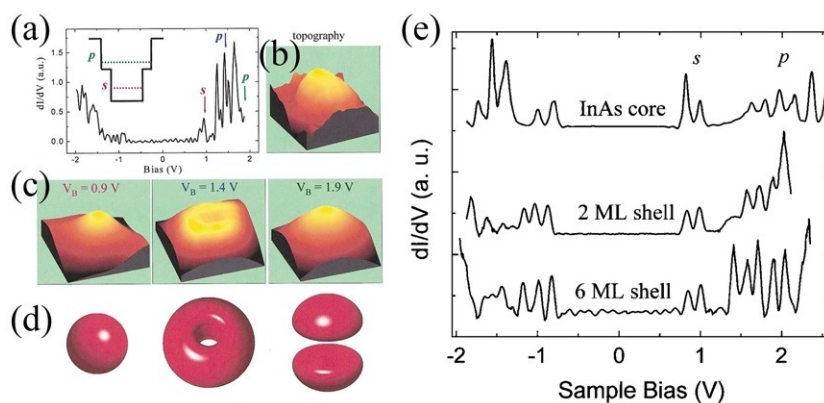


Figure 24. Wave function imaging and calculation for an InAs/ZnSe core/shell QD having a 6 ML shell. (a) A tunneling spectrum acquired for the nanocrystal. (b) $8 \times 8 \text{ nm}^2$ topographic image. (c) Current images obtained simultaneously with the topographic scan at three different bias values denoted by arrows in (a). (d) Isoprobability surfaces, showing s^2 (left), $p_x^2 + p_y^2$ (center), and p_z^2 (right). (e) Tunneling conductance spectra of an InAs core QD (numerical derivative) and two core/shell nanocrystals with two (numerical derivative) and six (lock-in method) ML shells with nominal core radii $\sim 1.7 \text{ nm}$.^[58] These figures are taken from Ref. [58] with permission.

theoretical prediction, which is caused by the delocalization of the carrier wave function in the core/shell structure.^[175] However, due to the Fermi level shift, the discontinuity of the effective mass and the difference of the dielectric constant at the core/shell interface, the effect of increasing the outer diameter of the core/shell on the PbSe size is smaller than that of increasing the size of a single PbSe.

The simultaneous existence of electrons and holes may result in electron-hole attraction and spin interaction.^[176] The premise of this research is to be able to separate the electron and hole current and measure the electron-hole interaction. Swart et al.^[177] analysis of PbSe/CdSe core/shell QDs shows that the system can meet the above conditions, because its hole energy level is in the PbSe core, while the electron energy level is delocalized in the whole heterostructure. Therefore, holes can be injected into the core at a low bias voltage, resulting in hole-induced electron tunneling. At the same time, the hole current is strongly suppressed due to the higher potential barrier and larger hole effective mass in CdSe. In addition, the experiment proves that two different tunneling channels exist simultaneously, namely, normal single-electron tunneling and hole-induced single-electron tunneling. By capturing a positively charged hole in the core of the QD, compared with the neutral QD, an additional electron transmission channel is opened at a lower applied bias voltage. The bias voltage difference between the new and traditional tunneling channel directly gives the electron-hole interaction energy of each electron level. This result is of great significance to electrically controlled single photon emission.

4.4.2. Quantum Dots/Nanorod Core/Shell Structure Nanocrystals

In addition to taking the material as a parameter for the study of core/shell heterostructure, the dependence of its properties on topography and structure can also be studied. Steiner et al.^[178] studied the core/shell structure of CdSe/CdS and ZnSe/CdS QDs/nanorods using STM. Figure 25(d) shows the dI/dV spectra obtained at different positions on a single CdSe/CdS QD/nanorod at 4.2 K, and the corresponding theoretical curve is above the experimental results (red curve). Curves 1 and 2 are measured near one vertex and at the other end of the nanorod, respectively. Both show a single-particle band gap of about 2.9 eV, indicating that the band gap on CdS nanorods far enough from the CdSe core is almost constant. However, the results above the core show a significantly smaller band gap, as shown in curve 3, and both the ground state of the electron and hole are redshifted, and the ground state of the electron is less redshifted than hole. Consequently, the reduction of band gap of CdSe core relative to CdS shell is asymmetric, and the displacement of conduction band edge is small. To illustrate the generality of this method, they applied it to study ZnSe/CdS system. As shown in Figure 25(e), the band gap values observed along most areas of the nanorod are 2.7–2.9 eV (curves 1 and 2), which correspond to the CdS band gap and are in good agreement with the calculated band gap (2.7 eV) and optical absorption spectrum. However, a small band gap of about 2 eV was measured at position 3, indicating that this position is a ZnSe core. And this value is

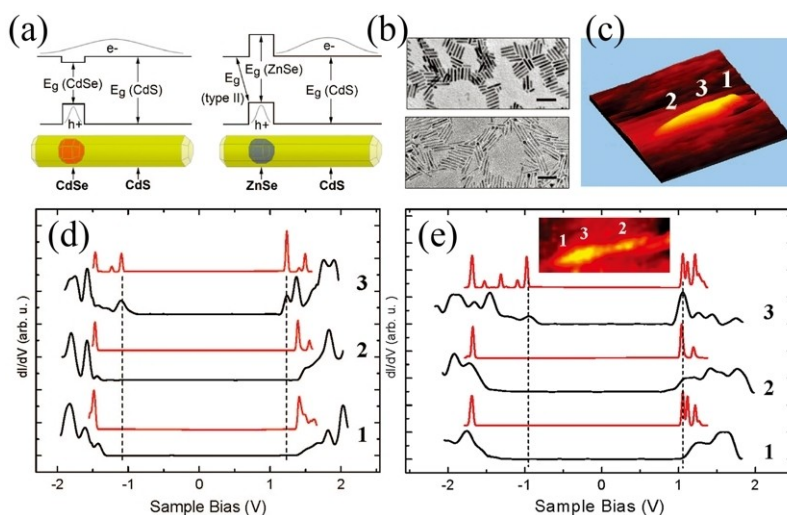


Figure 25. (a) Illustration of the (most common) previously predicted band structure and the electron and hole ground-state wave functions of type I CdSe/CdS (left) and type II ZnSe/CdS (right) QD/nanorods core/shell heterostructures. (b) TEM images of the CdSe/CdS (up) and ZnSe/CdS (bottom) core/shell nanorods. (c) 3D topographic STM image of the measured rod. (d) Three dI/dV vs V tunneling spectra, acquired at 4.2 K on a single CdSe/CdS nanocrystals at different locations (black curves). (e) Three experimental spectra (black lines), measured on the nanocrystals shown in the STM image presented in the inset. The positions where the spectra were acquired are marked near the rod. The corresponding calculated spectra are shown above the measured curves (red lines).^[178] These figures are taken from Ref. [178] with permission.

not consistent with the band gap of ZnSe but corresponds to the band gap of ZnSe/CdS system measured optically. Therefore, it can be determined that STS can obtain the direct information of the internal electrons of the core/shell structure nanocrystals, such as the determination of the energy band offset, etc., which provides useful data for tailoring the core/shell colloidal structure to meet the design of optoelectronic devices with specific optical and electrical properties.

4.4.3. Metal/Semiconductor Core/Shell Quantum Dots

So far, the research of STM and STS is mostly limited to uniform semiconductor QDs and semiconductor/semiconductor core/shell structure QDs. In contrast, there are relatively few studies on metal/semiconductor hybrid QDs. Steiner et al.^[179] explained the energy level change of metal/semiconductor junction in dumbbell-shaped Au/CdSe nanorods with low temperature STS. The work of Bekenstein et al.^[180] revealed the effect of Ru cage-like shell on Cu₂S semiconductor core. Tuhin Shuvra Basu et al.^[181] synthesized nearly monodisperse spherical metal/semiconductor Au/ZnS QDs using spherical Au nano-core as raw materials by simple wet chemical method. The method is to first synthesize Au nano-core, then coat a thin layer of Ag nano-shell on the nano-core, then convert the thin Ag layer into amorphous Ag₂S layer, and finally convert the Au/Ag₂S nanostructure into Au/ZnS QDs through cation exchange reaction. The electronic structure of a single nanocrystal in each step of the preparation process from

Au nanocrystals to final Au/ZnS QDs was analyzed at 300 mK. As shown in Figure 26(a–b), STS results show that there is obvious Coulomb blockade effect in both single metal and bimetallic QDs (Au and Au/Ag QDs). For Ag₂S coated Au nanoparticles, the band gap increases owing to the existence of amorphous Ag₂S as a tunneling barrier. For Au/ZnS QDs, STS under the condition of “shell-tunneling” shows obvious quantum confinement effect. This study has promoted the understanding of single charge transport in metal/semiconductor QD and has important guiding significance for the synthesis of specific quantum in single electronic devices.

4.5. Other Colloidal Quantum Dots

Although most of the work on QD tunneling spectrum is concentrated in the three QD systems of InAs, CdSe and PbX, this versatile technique can be used to study the energy level structure of almost any colloidal nanocrystalline material. Silicon nanocrystals have attracted great interest because of their application in the field of optoelectronics. Zakonon et al.^[182] studied the electronic energy level structure and single electron charge effect of a single Si QD at room temperature using STM. They found that the STS spectrum of QDs with a diameter of about 4.3 nm has a 12-fold multi-step structure, which is in good agreement with the first level degeneracy expected by theoretical calculations.^[183] Rosso-Vasic et al.^[184] synthesized Si QDs with smaller size (1.57 ± 0.24 nm) and carried out STS measurements. The band gap obtained is

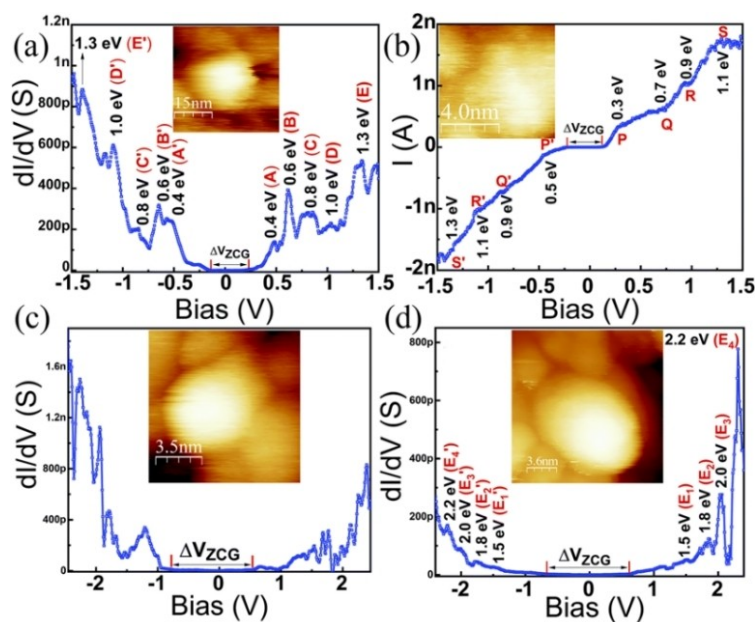


Figure 26. STS measurements of the individual (a) Au nanocrystals and (b) Au/Ag core/shell nanocrystals. STS measurements of (c) core/shell Au/Ag₂S nanocrystals and (d) core/shell Au/ZnS QD.^[181] These figures are taken from Ref. [181] with permission.

consistent with the optical absorption data, about 4 eV. Millo Group^[185] has studied the change of electronic energy level structure of surface functionalized colloidal silicon nanocrystals with their size by STS. The tunneling spectrum shows the quantum confinement effect that the band gap increases with the decrease of the size of nanoparticles. For NH₄Br or allylamine functionalized samples, the tunneling spectrum results show a similar behavior that the band edge of p-type doping moves towards a higher energy direction. It is one of the research hotspots of the application of Si QDs in optoelectronic and solar cell devices to change their electrical properties by adjusting the size and surface functionalization QDs. Millo and Ashkenazi et al.^[186] studied the electrical properties of boron and phosphorus codoped Si nanocrystals using STS, and found that the band gap changed from ~1.4 to ~1.8 eV, and the tunneling spectrum showed that two new states appeared in the original band gap, one near the edge of the conduction band, the other near the edge of the valence band, which actually came from the doped energy levels of P and B. The energy gap between these impurity states decreases with the increase of the QD diameter. Therefore, in addition to size, co-doping can also be effectively used to adjust the electronic properties of nanocrystals.

Moreover, aiming at the problem of quantum confinement in Ge nanocrystals, Millo et al.^[187] studied the relationship between the electronic structure of a single Ge nanocrystal and its size using STS, and found that the band gap width of Ge nanocrystals increased with the decrease of size, thus providing direct evidence of quantum confinement effect in Ge nanocrystals.

Due to the existence of Cu vacancies, Cu₂S compounds have both quantum confinement and natural electron doping, so these compounds may have important applications in optoelectronic technology.^[188,189] The formation of Cu vacancy in Cu₂S nanocrystals can be achieved through various approaches including oxidation in ambient atmosphere,^[190,191] chemical treatment^[192,193] and moderate heat treatment.^[189,194] Kathy Vinokurov et al.^[195] studied the change of energy band structure of Cu₂S nanocrystals during oxidation to form Cu_{2-x}S phase through STM. Oxidation led to the appearance of gap states near the valence band, and the Fermi energy level shifted slightly to the edge of the valence band, like p-type doping. Bekenstein et al.^[189] doped Cu₂S nanocrystalline arrays with medium temperature (T < 400 K) heat treatment and studied the copper vacancy formed after doping by STM. Unlike the equivalent doping method of introducing alternative or interstitial impurities, the thermal doping method will not introduce additional impurities into the nanocrystals. The unique medium-temperature thermal doping conditions of these nanocrystals allow the nanocrystalline film to be patterned and doped by local heating of the focused laser

beam, thus making nanocrystalline devices with good performance.

5. Summary and Prospect

Colloidal QDs not only have unique optical and electrical characteristics, but also have the advantages of controllable size and shape, low synthesis cost, and the potential for large-scale production. They play a vital role in emerging laser technology, special optoelectronic devices, and biological fluorescence labeling and other fields. The core/shell system is of great significance in the field of colloidal nanoscience. The study and application of core/shell structures have advanced the development of colloidal nanocrystal heterostructures, whose electronic and optical properties can be controlled by quantum confinement and realized by epitaxially connecting two semiconductor phases within a single colloidal nanoparticle. In addition to chemical stability, the shape, size, and surface modification of core/shell QDs play a vital role in the carrier confinement resulting in a wide range of optoelectronic applications such as solar cells, light-emitting diodes (LEDs), luminescent solar concentrators (LSCs), etc. Based on the systematic reviews and analyses on the research stream, this review article provides abundant information for the research and development of nanoscale optoelectronic devices and sensors in the future. However, it is not difficult to find that there are still many open problems in the study of colloidal QDs using STM:

1. There are two kinds of tunneling models, “shell-tunneling” and “shell-filling”. The research of the former is complete, and the interpretation of the tunneling spectrum obtained under the condition is detailed. However, the latter requires high bias voltage conditions, which makes the DBTJ unstable and difficult to obtain repeatable and undisturbed experimental results. Consequently, there are few studies on the “shell-filled” tunneling spectrum and interpreting the tunneling spectrum under this condition faces a great challenge.
2. The tunneling spectrum obtained by DBTJ is mostly focused on the interpretation of the resonance peak obtained under positive bias voltage, and only a few literatures analyze the resonance peak obtained under negative bias voltage.
3. For the energy level structure of colloidal QDs, most of the research groups focus on the S and P states, while there are many gaps in the research of higher states.
4. At present, the research on colloidal QDs with core/shell structure is less than that of single-component QDs, and the research system is not perfect. There are few studies on energy level structure, multi-electron tunneling process and its electro-phonon coupling.

5. The current research has focused on the static energy level structure of QDs and has not studied the dynamic changes of electronic structure during their formation. It is necessary to obtain the dynamic electronic structure of the formation process of core/shell QDs to reveal the interaction between the core/shell electronic structures.

STM is a critical method to study the electrical properties of low-dimensional nanomaterials such as QDs. It can not only obtain the electronic density of state distribution at the fixed position of the sample, and then obtain the electronic structure information of the sample, but also obtain the spatial distribution of the LDOS at a specific energy, which promotes understanding of the physical properties of QDs. Nonetheless, new types of QDs have emerged within the last decade, and perovskite^[196] and carbon-based QDs^[197] are famous examples. Almost all these categories can be synthesized in both polar and non-polar solvents with different colloidal/deposition approaches. It can be predicted that with the continuous synthesis of colloidal QDs with new crystal structures, an increasing number of researchers will focus on the heterostructure of colloidal QDs synthesized by two or more materials. Compared with traditional colloidal QDs, it is more stable and has higher fluorescence efficiency. The research on the physical properties of such QDs is the prerequisite to promote its extensive application. Scanning tunnelling microscopy and spectroscopy will be an appropriate tool for investigating these materials in detail. Because the methodology is general and can in principle be used to investigate nanocrystals of any composition and shape.

References

- [1] V. I. Klimov, *Annu. Rev. Phys. Chem.* **2007**, *58*, 635–673.
- [2] B. J. T. Victor, I. Klimov, *Nanocrystal Quantum Dots*, CRC Press, **2017**.
- [3] S. V. Gaponenko, *Optical Properties of Semiconductor Nanocrystals*, Cambridge University Press, Cambridge, **1998**.
- [4] D. V. Talapin, J.-S. Lee, M. V. Kovalenko, E. V. Shevchenko, *Chem. Rev.* **2010**, *110*, 389–458.
- [5] L. E. Brus, *J. Chem. Phys.* **1984**, *80*, 4403–4409.
- [6] A. P. Alivisatos, *Science* **1996**, *271*, 933–937.
- [7] C.-H. Chuang, C. Burda, *J. Phys. Chem. Lett.* **2012**, *3*, 1921–1927.
- [8] D. A. Wheeler, J. Z. Zhang, *Adv. Mater.* **2013**, *25*, 2878–2896.
- [9] R. C. Ashoori, *Nature* **1996**, *379*, 413–419.
- [10] M. A. Kastner, *Phys. Today* **1993**, *46*, 24–31.
- [11] P. Kambhampati, *J. Phys. Chem. C* **2011**, *115*, 22089–22109.
- [12] O. Chen, J. Zhao, V. P. Chauhan, J. Cui, C. Wong, D. K. Harris, H. Wei, H.-S. Han, D. Fukumura, R. K. Jain, M. G. Bawendi, *Nat. Mater.* **2013**, *12*, 445–451.
- [13] M. Nirmal, L. Brus, *Acc. Chem. Res.* **1999**, *32*, 407–414.
- [14] Z. Ding, B. M. Quinn, S. K. Haram, L. E. Pell, B. A. Korgel, A. J. Bard, *Science* **2002**, *296*, 1293–1297.
- [15] A. P. Litvin, I. V. Martynenko, F. Purcell-Milton, A. V. Baranov, A. V. Fedorov, Y. K. Gun'ko, *J. Mater. Chem. A* **2017**, *5*, 13252–13275.
- [16] R. Rossetti, S. Nakahara, L. E. Brus, *J. Chem. Phys.* **1983**, *79*, 1086–1088.
- [17] C. M. Niemeyer, *Angew. Chem. Int. Ed.* **2001**, *40*, 4128–4158.
- [18] J. Tian, G. Cao, *Nano Rev* **2013**, *4*, 22578.
- [19] J. M. Luther, J. Gao, M. T. Lloyd, O. E. Semonin, M. C. Beard, A. J. Nozik, *Adv. Mater.* **2010**, *22*, 3704–3707.
- [20] A. G. Pattantyus-Abraham, I. J. Kramer, A. R. Barkhouse, X. Wang, G. Konstantatos, R. Debnath, L. Levina, I. Raabe, M. K. Nazeeruddin, M. Grätzel, E. H. Sargent, *ACS Nano* **2010**, *4*, 3374–3380.
- [21] G. Konstantatos, I. Howard, A. Fischer, S. Hoogland, J. Clifford, E. Klem, L. Levina, E. H. Sargent, *Nature* **2006**, *442*, 180–183.
- [22] V. Medvedev, M. Kazes, S. Kan, U. Banin, Y. Talmon, N. Tessler, *Synth. Met.* **2003**, *137*, 1047–1048.
- [23] A. V. Malko, A. A. Mikhailovsky, M. A. Petruska, J. A. Hollingsworth, H. Htoon, M. G. Bawendi, V. I. Klimov, *Appl. Phys. Lett.* **2002**, *81*, 1303–1305.
- [24] M. Kazes, D. Y. Lewis, U. Banin, *Adv. Funct. Mater.* **2004**, *14*, 957–962.
- [25] S. Koley, J. Cui, Y. E. Panfil, U. Banin, *Acc. Chem. Res.* **2021**, *54*, 1178–1188.
- [26] X. Gao, Y. Cui, R. M. Levenson, L. W. K. Chung, S. Nie, *Nat. Biotechnol.* **2004**, *22*, 969–976.
- [27] M. L. Schipper, G. Iyer, A. L. Koh, Z. Cheng, Y. Ebenstein, A. Aharoni, S. Keren, L. A. Bentolila, J. Li, J. Rao, X. Chen, U. Banin, A. M. Wu, R. Sinclair, S. Weiss, S. S. Gambhir, *Small* **2009**, *5*, 126–134.
- [28] J. R. Cole, N. A. Mirin, M. W. Knight, G. P. Goodrich, N. J. Halas, *J. Phys. Chem. C* **2009**, *113*, 12090–12094.
- [29] L. Li, T. J. Daou, I. Texier, T. T. Kim Chi, N. Q. Liem, P. Reiss, *Chem. Mater.* **2009**, *21*, 2422–2429.
- [30] I. L. Medintz, H. T. Uyeda, E. R. Goldman, H. Mattoussi, *Nat. Mater.* **2005**, *4*, 435–446.
- [31] J. J. Li, Y. A. Wang, W. Guo, J. C. Keay, T. D. Mishima, M. B. Johnson, X. Peng, *J. Am. Chem. Soc.* **2003**, *125*, 12567–12575.
- [32] L. Brus, *J. Phys. Chem.* **1986**, *90*, 2555–2560.
- [33] D. J. Norris, M. G. Bawendi, *Phys. Rev. B* **1996**, *53*, 16338–16346.
- [34] K. Overgaag, P. Liljeroth, B. Grandidier, D. Vanmaekelbergh, *ACS Nano* **2008**, *2*, 600–606.
- [35] D. Steiner, A. Aharoni, U. Banin, O. Millo, *Nano Lett.* **2006**, *6*, 2201–5.
- [36] G. Binnig, H. Rohrer, Ch. Gerber, E. Weibel, *Appl. Phys. Lett.* **1982**, *40*, 178–180.
- [37] G. Binnig, H. Rohrer, *Rev. Mod. Phys.* **1987**, *59*, 615–625.
- [38] J. Tersoff, D. R. Hamann, *Phys. Rev. B* **1985**, *31*, 805–813.
- [39] J. Repp, G. Meyer, F. E. Olsson, M. Persson, *Science* **2004**, *305*, 493–495.

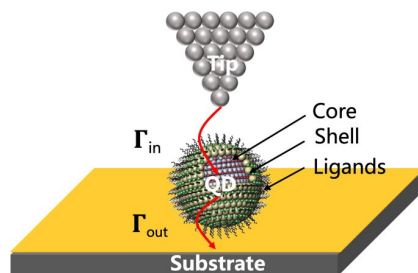
- [40] F. E. Olsson, M. Persson, A. G. Borisov, J.-P. Gauyacq, J. Lagoute, S. Fölsch, *Phys. Rev. Lett.* **2004**, *93*, 206803.
- [41] A. J. Heinrich, J. A. Gupta, C. P. Lutz, D. M. Eigler, *Science* **2004**, *306*, 466–469.
- [42] M. Berthe, A. Urbietta, L. Perdigão, B. Grandidier, D. Deresmes, C. Delerue, D. Stiévenard, R. Rurali, N. Lorente, L. Magaud, P. Ordejón, *Phys. Rev. Lett.* **2006**, *97*, 206801.
- [43] J. Repp, G. Meyer, S. Paavilainen, F. E. Olsson, M. Persson, *Phys. Rev. Lett.* **2005**, *95*, 225503.
- [44] J. Repp, G. Meyer, S. M. Stojković, A. Gourdon, C. Joachim, *Phys. Rev. Lett.* **2005**, *94*, 026803.
- [45] X. H. Qiu, G. V. Nazin, W. Ho, *Phys. Rev. Lett.* **2004**, *92*, 206102.
- [46] S. W. Wu, G. V. Nazin, X. Chen, X. H. Qiu, W. Ho, *Phys. Rev. Lett.* **2004**, *93*, 236802.
- [47] X. Lu, M. Grobis, K. H. Khoo, S. G. Louie, M. F. Crommie, *Phys. Rev. Lett.* **2003**, *90*, 096802.
- [48] N. A. Pradhan, N. Liu, C. Silien, W. Ho, *Phys. Rev. Lett.* **2005**, *94*, 076801.
- [49] U. Banin, Y. Cao, D. Katz, O. Millo, *Nature* **1999**, *400*, 542–544.
- [50] L. Jdira, K. Overgaag, J. Gerritsen, D. Vanmaekelbergh, P. Liljeroth, S. Speller, *Nano Lett.* **2008**, *8*, 4014–4019.
- [51] D. Katz, T. Wizansky, O. Millo, E. Rothenberg, T. Mokari, U. Banin, *Phys. Rev. Lett.* **2002**, *89*, 086801.
- [52] O. Millo, D. Katz, Y. Cao, U. Banin, *Phys. Rev. B* **2000**, *61*, 16773–16777.
- [53] O. Millo, D. Katz, Y. Levi, Y. W. Cao, U. Banin, *J. Low Temp. Phys.* **2000**, *118*, 365–373.
- [54] E. P. A. M. Bakkers, D. Vanmaekelbergh, *Phys. Rev. B* **2000**, *62*, R7743–R7746.
- [55] Z. Hens, D. Vanmaekelbergh, E. J. Stoffels, H. van Kempen, *Phys. Rev. Lett.* **2002**, *88*, 2368031–2368034.
- [56] D. Katz, O. Millo, S.-H. Kan, U. Banin, *Appl. Phys. Lett.* **2001**, *79*, 117–119.
- [57] E. P. A. M. Bakkers, Z. Hens, L. P. Kouwenhoven, L. Gurevich, D. Vanmaekelbergh, *Nanotechnology* **2002**, *13*, 304.
- [58] O. Millo, D. Katz, Y. Cao, U. Banin, *Phys. Rev. Lett.* **2001**, *86*, 5751–5754.
- [59] B. Alpers, I. Rubinstein, G. Hodes, D. Porath, O. Millo, *Appl. Phys. Lett.* **1999**, *75*, 1751–1753.
- [60] P. Liljeroth, K. Overgaag, A. Urbietta, B. Grandidier, S. G. Hickey, D. Vanmaekelbergh, *Phys. Rev. Lett.* **2006**, *97*, 096803.
- [61] V. Notot, W. Walravens, M. Berthe, N. Peric, A. Addad, X. Wallart, C. Delerue, Z. Hens, B. Grandidier, L. Biadala, *ACS Nano* **2022**, *16*, 3081–3091.
- [62] D. A. Kislitsyn, C. F. Gervasi, T. Allen, P. K. B. Palomaki, J. D. Hackley, R. Maruyama, G. V. Nazin, *J. Phys. Chem. Lett.* **2014**, *5*, 3701–3707.
- [63] C. F. Gervasi, D. A. Kislitsyn, T. L. Allen, J. D. Hackley, R. Maruyama, G. V. Nazin, *Nanoscale* **2015**, *7*, 19732–19742.
- [64] S. T. Ueda, I. Kwak, A. Abelson, S. Wolf, C. Qian, M. Law, A. C. Kummel, *Appl. Surf. Sci.* **2020**, *513*, 145812.
- [65] G. A. Grinbom, M. Saraf, C. Saguy, A. C. Bartnik, F. Wise, E. Lifshitz, *Phys. Rev. B* **2010**, *81*, 245301.
- [66] U. Banin, O. Millo, *Annu. Rev. Phys. Chem.* **2003**, *54*, 465–492.
- [67] C. de M Donegá, *Chem. Soc. Rev.* **2011**, *40*, 1512–1546.
- [68] S. Kano, T. Tada, Y. Majima, *Chem. Soc. Rev.* **2015**, *44*, 970–987.
- [69] J. M. Pietryga, Y.-S. Park, J. Lim, A. F. Fidler, W. K. Bae, S. Brovelli, V. I. Klimov, *Chem. Rev.* **2016**, *116*, 10513–10622.
- [70] T. Kim, S. Park, S. Jeong, *Nat. Commun.* **2021**, *12*, 3013.
- [71] X. Shan, Y. Zhou, B. Li, Z. Zeng, B. Ji, *Chem. Mater.* **2023**, *35*, 2569–2578.
- [72] W. Koh, S. H. Choi, Y. Kim, H. Kim, K. K. Kim, S. Jeong, *Adv. Photonics Res* **2022**, *3*, 2100243.
- [73] T. Zhao, Q. Zhao, J. Lee, S. Yang, H. Wang, M.-Y. Chuang, Y. He, S. M. Thompson, G. Liu, N. Oh, C. B. Murray, C. R. Kagan, *Chem. Mater.* **2022**, *34*, 8306–8315.
- [74] D. H. Kwak, P. Ramasamy, Y. S. Lee, M. H. Jeong, J. S. Lee, *ACS Appl. Mater. Interfaces* **2019**, *11*, 29041–29046.
- [75] J. Leemans, V. Pejović, E. Georgitzikis, M. Minjauw, A. B. Siddik, Y. Deng, Y. Kuang, G. Roelkens, C. Detavernier, I. Lieberman, P. E. Malinowski, D. Cheyns, Z. Hens, *Adv. Sci.* **2022**, *9*, 2200844.
- [76] B. Sun, A. M. Najarian, L. K. Sagar, M. Biondi, M. Choi, X. Li, L. Levina, S. Baek, C. Zheng, S. Lee, A. R. Kirmani, R. Sabatini, J. Abed, M. Liu, M. Vafaie, P. Li, L. J. Richter, O. Voznyy, M. Chekini, Z. Lu, F. P. García de Arquer, E. H. Sargent, *Adv. Mater.* **2022**, *34*, 2203039.
- [77] X. Zhao, L. J. Lim, S. S. Ang, Z. Tan, *Adv. Mater.* **2022**, *34*, 2206409.
- [78] X. Liu, Y. Ai, Q. Chen, S. Liu, *Mater. Sci. Semicond. Process.* **2021**, *121*, 105365.
- [79] H. Tang, J. Zhong, W. Chen, K. Shi, G. Mei, Y. Zhang, Z. Wen, P. Müller-Buschbaum, D. Wu, K. Wang, X. W. Sun, *ACS Appl. Nano Mater.* **2019**, *2*, 6135–6143.
- [80] A. Abelson, C. Qian, Z. Crawford, G. T. Zimanyi, M. Law, *Nano Lett.* **2022**, *22*, 9578–9585.
- [81] R. Schwanninger, S. M. Koepfli, O. Yarema, A. Dorodnyy, M. Yarema, A. Moser, S. Nashashibi, Y. Fedoryshyn, V. Wood, J. Leuthold, *ACS Appl. Mater. Interfaces* **2023**, *15*, 10847–10857.
- [82] X. Liang, Y. Liu, P. Liu, J. Yang, J. Liu, Y. Yang, B. Wang, J. Hu, L. Zhang, G. Yang, S. Lu, G. Liang, X. Lan, J. Zhang, L. Gao, J. Tang, *Sci. Bull.* **2023**, *68*, 698–705.
- [83] M. Peng, Y. Liu, F. Li, X. Hong, Y. Liu, Z. Wen, Z. Liu, W. Ma, X. Sun, *ACS Appl. Mater. Interfaces* **2021**, *13*, 51198–51204.
- [84] J. Yang, Y. Lv, Z. He, B. Wang, S. Chen, F. Xiao, H. Hu, M. Yu, H. Liu, X. Lan, H.-Y. Hsu, H. Song, J. Tang, *ACS Photonics* **2023**, DOI 10.1021/acsp Photonics.2c01145.
- [85] D. Bederak, A. Shulga, S. Kahmann, W. Talsma, J. Pelanskis, D. N. Dirin, M. V. Kovalenko, M. A. Loi, *Adv. Electron. Mater.* **2022**, *8*, 2101126.
- [86] S. Chan, M. Liu, K. Latham, M. Haruta, H. Kurata, T. Teranishi, Y. Tachibana, *J. Mater. Chem. C* **2017**, *5*, 2182–2187.
- [87] J. Müller, J. M. Lupton, A. L. Rogach, J. Feldmann, D. V. Talapin, H. Weller, *Phys. Rev. Lett.* **2004**, *93*, 167402.

- [88] M. Shim, C. Wang, D. J. Norris, P. Guyot-Sionnest, *MRS Bull.* **2001**, *26*, 1005–1008.
- [89] R. L. Whetten, J. T. Khoury, M. M. Alvarez, S. Murthy, I. Vezmar, Z. L. Wang, P. W. Stephens, C. L. Cleveland, W. D. Luedtke, U. Landman, *Adv. Mater.* **1996**, *8*, 428–433.
- [90] C. T. Black, C. B. Murray, R. L. Sandstrom, S. Sun, *Science* **2000**, *290*, 1131–1134.
- [91] M. P. Pileni, *J. Phys. Chem. B* **2001**, *105*, 3358–3371.
- [92] A. P. Alivisatos, K. P. Johnsson, X. Peng, T. E. Wilson, C. J. Loweth, M. P. Bruchez, P. G. Schultz, *Nature* **1996**, *382*, 609–611.
- [93] C. P. Collier, T. Vossmeier, J. R. Heath, *Annu. Rev. Phys. Chem.* **1998**, *49*, 371–404.
- [94] J. E. B. Katari, V. L. Colvin, A. P. Alivisatos, *J. Phys. Chem.* **1994**, *98*, 4109–4117.
- [95] C. B. Murray, C. R. Kagan, M. G. Bawendi, *Science* **1995**, *270*, 1335–1338.
- [96] V. Lesnyak, N. Gaponik, A. Eychmüller, *Chem. Soc. Rev.* **2013**, *42*, 2905–2929.
- [97] C. B. Murray, D. J. Norris, M. G. Bawendi, *J. Am. Chem. Soc.* **1993**, *115*, 8706–8715.
- [98] V. L. Colvin, M. C. Schlamp, A. P. Alivisatos, *Nature* **1994**, *370*, 354–357.
- [99] Z. A. Peng, X. Peng, *J. Am. Chem. Soc.* **2001**, *123*, 183–184.
- [100] Z. A. Peng, X. Peng, *J. Am. Chem. Soc.* **2001**, *123*, 1389–1395.
- [101] Z. A. Peng, X. Peng, *J. Am. Chem. Soc.* **2002**, *124*, 3343–3353.
- [102] J. Jasieniak, C. Bullen, J. van Embden, P. Mulvaney, *J. Phys. Chem. B* **2005**, *109*, 20665–20668.
- [103] J. Shamsi, A. S. Urban, M. Imran, L. De Trizio, L. Manna, *Chem. Rev.* **2019**, *119*, 3296–3348.
- [104] C. B. Murray, C. R. Kagan, M. G. Bawendi, *Annu. Rev. Mater. Sci.* **2000**, *30*, 545–610.
- [105] L. Liu, Z. Zhuang, T. Xie, Y.-G. Wang, J. Li, Q. Peng, Y. Li, *J. Am. Chem. Soc.* **2009**, *131*, 16423–16429.
- [106] X. Peng, *Adv. Mater.* **2003**, *15*, 459–463.
- [107] M. A. Hines, P. Guyot-Sionnest, *J. Phys. Chem.* **1996**, *100*, 468–471.
- [108] E. Roduner, *Chem. Soc. Rev.* **2006**, *35*, 583.
- [109] A. P. Alivisatos, *J. Phys. Chem.* **1996**, *100*, 13226–13239.
- [110] P. Ball, L. Garwin, *Nature* **1992**, *355*, 761–764.
- [111] M. G. Bawendi, W. L. Wilson, L. Rothberg, P. J. Carroll, T. M. Jedju, M. L. Steigerwald, L. E. Brus, *Phys. Rev. Lett.* **1990**, *65*, 1623–1626.
- [112] A. I. Ekimov, A. L. Efros, A. A. Onushchenko, *Solid State Commun.* **1985**, *56*, 921–924.
- [113] R. Rossetti, L. Brus, *J. Phys. Chem.* **1982**, *86*, 4470–4472.
- [114] L. E. Brus, *J. Chem. Phys.* **1983**, *79*, 5566–5571.
- [115] C. R. Kagan, E. Lifshitz, E. H. Sargent, D. V. Talapin, *Science* **2016**, *353*, aac5523.
- [116] V. L. Colvin, A. N. Goldstein, A. P. Alivisatos, *J. Am. Chem. Soc.* **1992**, *114*, 5221–5230.
- [117] M. Brust, R. Etchenique, E. J. Calvo, G. J. Gordillo, *Chem. Commun.* **1996**, 1949–1950.
- [118] Z. Sun, I. Swart, C. Delerue, D. Vanmaekelbergh, P. Liljeroth, *Phys. Rev. Lett.* **2009**, *102*, 196401.
- [119] D. Steiner, D. Azulay, A. Aharoni, A. Salant, U. Banin, O. Millo, *Nanotechnology* **2008**, *19*, 065201.
- [120] I. Swart, P. Liljeroth, D. Vanmaekelbergh, *Chem. Rev.* **2016**, *116*, 11181–11219.
- [121] E. P. A. M. Bakkers, Z. Hens, A. Zunger, A. Franceschetti, L. P. Kouwenhoven, L. Gurevich, D. Vanmaekelbergh, *Nano Lett.* **2001**, *1*, 551–556.
- [122] P. Liljeroth, L. Jdira, K. Overgaag, B. Grandidier, S. Speller, D. Vanmaekelbergh, *Phys. Chem. Chem. Phys.* **2006**, *8*, 3845.
- [123] M. R. Hummon, A. J. Stollenwerk, V. Narayanamurti, P. O. Anikeeva, M. J. Panzer, V. Wood, V. Bulović, *Phys. Rev. B* **2010**, *81*, 115439.
- [124] M. Lannoo, C. Delerue, G. Allan, *Phys. Rev. Lett.* **1995**, *74*, 3415–3418.
- [125] A. Franceschetti, A. Williamson, A. Zunger, *J. Phys. Chem. B* **2000**, *104*, 3398–3401.
- [126] D. V. Averin, A. N. Korotkov, K. K. Likharev, *Phys. Rev. B* **1991**, *44*, 6199–6211.
- [127] Y. M. Niquet, C. Delerue, G. Allan, M. Lannoo, *Phys. Rev. B: Condens. Matter Mater. Phys.* **2002**, *65*, 1–14.
- [128] M. Nirmal, B. O. Dabbousi, M. G. Bawendi, J. J. Macklin, J. K. Trautman, T. D. Harris, L. E. Brus, *Nature* **1996**, *383*, 802–804.
- [129] W. G. J. H. M. van Sark, P. L. T. M. Frederix, D. J. Van den Heuvel, H. C. Gerritsen, A. A. Bol, J. N. J. van Lingen, C. de Mello Donegá, A. Meijerink, *J. Phys. Chem. B* **2001**, *105*, 8281–8284.
- [130] M. Bayer, P. Hawrylak, K. Hinzer, S. Fafard, M. Korkusinski, Z. R. Wasilewski, O. Stern, A. Forchel, *Science* **2001**, *291*, 451–453.
- [131] S. Empedocles, M. Bawendi, *Acc. Chem. Res.* **1999**, *32*, 389–396.
- [132] T. S. Basu, S. Diesch, E. Scheer, *Nanoscale* **2018**, *10*, 13949–13958.
- [133] T. Maltezopoulos, A. Bolz, C. Meyer, C. Heyn, W. Hansen, M. Morgenstern, R. Wiesendanger, *Phys. Rev. Lett.* **2003**, *91*, 196804.
- [134] D. Mocatta, G. Cohen, J. Schattner, O. Millo, E. Rabani, U. Banin, *Science* **2011**, *332*, 77–81.
- [135] A. J. Morris-Cohen, M. D. Donakowski, K. E. Knowles, E. A. Weiss, *J. Phys. Chem. C* **2010**, *114*, 897–906.
- [136] N. Guijarro, T. Lana-Villarreal, I. Mora-Seró, J. Bisquert, R. Gómez, *J. Phys. Chem. C* **2009**, *113*, 4208–4214.
- [137] G. Kalyuzhny, R. W. Murray, *J. Phys. Chem. B* **2005**, *109*, 7012–7021.
- [138] E. D. Goodwin, B. T. Diroll, S. J. Oh, T. Paik, C. B. Murray, C. R. Kagan, *J. Phys. Chem. C* **2014**, *118*, 27097–27105.
- [139] A. M. Munro, I. Jen-La Plante, M. S. Ng, D. S. Ginger, *J. Phys. Chem. C* **2007**, *111*, 6220–6227.
- [140] L. A. King, D. J. Riley, *J. Phys. Chem. C* **2012**, *116*, 3349–3355.
- [141] G. Li, V. Shrotriya, J. Huang, Y. Yao, T. Moriarty, K. Emery, Y. Yang, *Nat. Mater.* **2005**, *4*, 864–868.
- [142] Y. Shen, M. Y. Gee, R. Tan, P. J. Pellechia, A. B. Greytak, *Chem. Mater.* **2013**, *25*, 2838–2848.
- [143] M. Soreni-Harari, N. Yaacobi-Gross, D. Steiner, A. Aharoni, U. Banin, O. Millo, N. Tessler, *Nano Lett.* **2008**, *8*, 678–684.

- [144] D. V. Talapin, J. Steckel, *MRS Bull.* **2013**, *38*, 685–691.
- [145] A. Llordés, G. Garcia, J. Gazquez, D. J. Milliron, *Nature* **2013**, *500*, 323–326.
- [146] S. Adachi, *Properties of Group-IV, III–V and II–VI Semiconductors*, John Wiley & Sons, Ltd, Chichester, UK, **2005**.
- [147] W. Liu, A. Y. Chang, R. D. Schaller, D. V. Talapin, *J. Am. Chem. Soc.* **2012**, *134*, 20258–20261.
- [148] T. Wang, R. Vaxenburg, W. Liu, S. M. Rupich, E. Lifshitz, A. L. Efros, D. V. Talapin, S. J. Sibener, *ACS Nano* **2015**, *9*, 725–732.
- [149] Z. Quan, J. Fang, *Nano Today* **2010**, *5*, 390–411.
- [150] D. Vanmaekelbergh, *Nano Today* **2011**, *6*, 419–437.
- [151] W. van der Stam, A. P. Gantapara, Q. A. Akkerman, G. Soligno, J. D. Meeldijk, R. van Roij, M. Dijkstra, C. de Mello Donega, *Nano Lett.* **2014**, *14*, 1032–1037.
- [152] J. L. Peters, T. Altantzis, I. Lobato, M. A. Jazi, C. van Overbeek, S. Bals, D. Vanmaekelbergh, S. B. Sinai, *Chem. Mater.* **2018**, *30*, 4831–4837.
- [153] G. Maruccio, C. Meyer, T. Matsui, D. V. Talapin, S. G. Hickey, H. Weller, R. Wiesendanger, *Small* **2009**, *5*, 808–812.
- [154] G. Maruccio, M. Janson, A. Schramm, C. Meyer, T. Matsui, C. Heyn, W. Hansen, R. Wiesendanger, M. Rontani, E. Molinari, *Nano Lett.* **2007**, *7*, 2701–2706.
- [155] G. Bester, A. Zunger, *Phys. Rev. B* **2005**, *71*, 045318.
- [156] L. Jdira, K. Overgaag, R. Stuiufuc, B. Grandidier, C. Delerue, S. Speller, D. Vanmaekelbergh, *Phys. Rev. B* **2008**, *77*, 205308.
- [157] P. Liljeroth, P. A. Z. van Emmichoven, S. G. Hickey, H. Weller, B. Grandidier, G. Allan, D. Vanmaekelbergh, *Phys. Rev. Lett.* **2005**, *95*, 086801.
- [158] I. Kang, F. W. Wise, *Journal of the Optical Society of America B* **1997**, *14*, 1632.
- [159] A. D. Andreev, A. A. Lipovskii, *Phys. Rev. B* **1999**, *59*, 15402–15404.
- [160] F. W. Wise, *Acc. Chem. Res.* **2000**, *33*, 773–780.
- [161] J. M. An, A. Franceschetti, S. V. Dudiy, A. Zunger, *Nano Lett.* **2006**, *6*, 2728–2735.
- [162] G. Nootz, L. A. Padilha, P. D. Olszak, S. Webster, D. J. Hagan, E. W. Van Stryland, L. Levina, V. Sukhovatkin, L. Brzozowski, E. H. Sargent, *Nano Lett.* **2010**, *10*, 3577–3582.
- [163] J. J. Peterson, L. Huang, C. Delerue, G. Allan, T. D. Krauss, *Nano Lett.* **2007**, *7*, 3827–3831.
- [164] B. L. Wehrenberg, C. Wang, P. Guyot-Sionnest, *J. Phys. Chem. B* **2002**, *106*, 10634–10640.
- [165] H. Du, C. Chen, R. Krishnan, T. D. Krauss, J. M. Harbold, F. W. Wise, M. G. Thomas, J. Silcox, *Nano Lett.* **2002**, *2*, 1321–1324.
- [166] B. Diaconescu, L. A. Padilha, P. Nagpal, B. S. Swartzentruber, V. I. Klimov, *Phys. Rev. Lett.* **2013**, *110*, 127406.
- [167] A. Franceschetti, J. W. Luo, J. M. An, A. Zunger, *Phys. Rev. B* **2009**, *79*, 241311.
- [168] R. Koole, G. Allan, C. Delerue, A. Meijerink, D. Vanmaekelbergh, A. J. Houtepen, *Small* **2008**, *4*, 127–133.
- [169] C. B. Murray, S. Sun, W. Gaschler, H. Doyle, T. A. Berley, C. R. Kagan, *IBM J. Res. Dev.* **2001**, *45*, 47–56.
- [170] G. Allan, C. Delerue, *Phys. Rev. B* **2004**, *70*, 245321.
- [171] K. Overgaag, D. Vanmaekelbergh, P. Liljeroth, G. Mahieu, B. Grandidier, C. Delerue, G. Allan, *J. Chem. Phys.* **2009**, *131*, 224510.
- [172] A. H. Ip, S. M. Thon, S. Hoogland, O. Voznyy, D. Zhitomirsky, R. Debnath, L. Levina, L. R. Rollny, G. H. Carey, A. Fischer, K. W. Kemp, I. J. Kramer, Z. Ning, A. J. Labelle, K. W. Chou, A. Amassian, E. H. Sargent, *Nat. Nanotechnol.* **2012**, *7*, 577–582.
- [173] F. Meinardi, H. McDaniel, F. Carulli, A. Colombo, K. A. Velizhanin, N. S. Makarov, R. Simonutti, V. I. Klimov, S. Brovelli, *Nat. Nanotechnol.* **2015**, *10*, 878–885.
- [174] J. Kwak, W. K. Bae, D. Lee, I. Park, J. Lim, M. Park, H. Cho, H. Woo, D. Y. Yoon, K. Char, S. Lee, C. Lee, *Nano Lett.* **2012**, *12*, 2362–2366.
- [175] A. C. Bartnik, F. W. Wise, A. Kigel, E. Lifshitz, *Phys. Rev. B* **2007**, *75*, 245424.
- [176] R. Hanson, L. P. Kouwenhoven, J. R. Petta, S. Tarucha, L. M. K. Vandersypen, *Rev. Mod. Phys.* **2007**, *79*, 1217–1265.
- [177] I. Swart, Z. Sun, D. Vanmaekelbergh, P. Liljeroth, *Nano Lett.* **2010**, *10*, 1931–1935.
- [178] D. Steiner, D. Dorfs, U. Banin, F. Della Sala, L. Manna, O. Millo, *Nano Lett.* **2008**, *8*, 2954–2958.
- [179] D. Steiner, T. Mokari, U. Banin, O. Millo, *Phys. Rev. Lett.* **2005**, *95*, 056805.
- [180] Y. Bekenstein, K. Vinokurov, U. Banin, O. Millo, *Nanotechnology* **2012**, *23*, 505710.
- [181] T. S. Basu, S. Diesch, R. Hayakawa, Y. Wakayama, E. Scheer, *Nanoscale* **2021**, *13*, 4978–4984.
- [182] B. Zaknoon, G. Bahir, C. Saguy, R. Edrei, A. Hoffman, R. A. Rao, R. Muralidhar, K.-M. Chang, *Nano Lett.* **2008**, *8*, 1689–1694.
- [183] F. A. Reboledo, A. Zunger, *Phys. Rev. B* **2000**, *62*, R2275–R2278.
- [184] M. Rosso-Vasic, E. Spruijt, Z. Popović, K. Overgaag, B. van Lagen, B. Grandidier, D. Vanmaekelbergh, D. Domínguez-Gutiérrez, L. De Cola, H. Zuillhof, *J. Mater. Chem.* **2009**, *19*, 5926.
- [185] O. Wolf, M. Dasog, Z. Yang, I. Balberg, J. G. C. Veinot, O. Millo, *Nano Lett.* **2013**, *13*, 2516–2521.
- [186] O. Ashkenazi, D. Azulay, I. Balberg, S. Kano, H. Sugimoto, M. Fujii, O. Millo, *Nanoscale* **2017**, *9*, 17884–17892.
- [187] O. Millo, I. Balberg, D. Azulay, T. K. Purkait, A. K. Swarnakar, E. Rivard, J. G. C. Veinot, *J. Phys. Chem. Lett.* **2015**, *6*, 3396–3402.
- [188] J. M. Luther, P. K. Jain, T. Ewers, A. P. Alivisatos, *Nat. Mater.* **2011**, *10*, 361–366.
- [189] Y. Bekenstein, K. Vinokurov, S. Keren-Zur, I. Hadar, Y. Schilt, U. Raviv, O. Millo, U. Banin, *Nano Lett.* **2014**, *14*, 1349–1353.
- [190] A. B. F. Martinson, S. C. Riha, E. Thimsen, J. W. Elam, M. J. Pellin, *Energy Environ. Sci.* **2013**, *6*, 1868–1878.
- [191] I. Kriegel, C. Jiang, J. Rodríguez-Fernández, R. D. Schaller, D. V. Talapin, E. da Como, J. Feldmann, *J. Am. Chem. Soc.* **2012**, *134*, 1583–1590.
- [192] P. K. Jain, K. Manthiram, J. H. Engel, S. L. White, J. A. Faucheaux, A. P. Alivisatos, *Angew. Chem.* **2013**, *125*, 13916–13920.

REVIEW

Colloidal quantum dots display remarkable optical and electrical characteristics with the potential for extensive applications in contemporary nanotechnology. This article presents a comprehensive review of the research advancements in measuring the electronic orbits and corresponding energy levels of colloidal quantum dots in various systems using Scanning tunneling microscopy and Scanning tunneling spectroscopy.



*J. Duan, J. Wang, L. Hou, P. Ji, W. Zhang, J. Liu, X. Zhu, Z. Sun, Y. Ma, L. Ma**

1 – 32

Application of Scanning Tunneling Microscopy and Spectroscopy in the Studies of Colloidal Quantum Qots